Monthly Notices of the ROYAL ASTRONOMICAL SOCIETY

MNRAS **515,** 473–490 (2022) https://doi.org/10.1093/mnras/stac1745
Advance Access publication 2022 June 24

Hard-X-ray-selected active galactic nuclei – II. Spectral energy distributions in the 5–45 GHz domain

Francesca Panessa [1★] Elia Chiaraluce [2] Gabriele Bruni [1★] Daniele Dallacasa,[3,4] Ari Laor,[5] Ranieri D. Baldi [4] Ehud Behar [5] Ian McHardy,[6] Francesco Tombesi[7,8,9,10,11] and Fausto Vagnetti[1,7]

[1]*INAF – Istituto di Astrofisica e Planetologia Spaziali, Via del Fosso del Cavaliere 100, I-00133 Roma, Italy*
[2]*AKKA Technologies Italia s.r.l., Via Tiburtina 1072/1074, I-00156 Roma, Italy*
[3]*DiFA – Dipartimento di Fisica e Astronomia, Università di Bologna, Via Piero Gobetti 93/2, I-40129 Bologna, Italy*
[4]*INAF – Istituto di Radioastronomia, Via Piero Gobetti 101, I-40129 Bologna, Italy*
[5]*Physics Department, The Technion, 32000 Haifa, Israel*
[6]*School of Physics and Astronomy, University of Southampton, Southampton SO17 1BJ, UK*
[7]*Dipartimento di Fisica, Università di Roma 'Tor Vergata', Via della Ricerca Scientifica 1, I-00133 Roma, Italy*
[8]*INAF – Astronomical Observatory of Rome, Via Frascati 33, I-00078 Monte Porzio Catone, Italy*
[9]*Department of Astronomy, University of Maryland, College Park, MD 20742, USA*
[10]*X-ray Astrophysics Laboratory, NASA/Goddard Space Flight Center, Greenbelt, MD 20771, USA*
[11]*INFN – Roma Tor Vergata, Via della Ricerca Scientifica 1, I-00133 Roma, Italy*

Accepted 2022 June 16. Received 2022 May 30; in original form 2022 March 1

ABSTRACT

A wide-frequency radio study of active galactic nuclei (AGN) is crucial to evaluate the intervening radiative mechanisms responsible for the observed emission and relate them with the underlying accretion physics. We present wide-frequency (5–45 GHz), high-sensitivity (few μJy beam^{-1}), (sub)-kpc Jansky Very Large Array (JVLA) observations of a sample of 30 nearby ($0.003 \leq z \leq 0.3$) AGN detected by the *International Gamma-Ray Astrophysics Laboratory* (*INTEGRAL*)/Imager on Board the *INTEGRAL* Satellite (IBIS) at hard X-ray. We find a high detection fraction of radio emission at all frequencies, i.e. ≥95 per cent at 5, 10, and 15 GHz and ≥80 per cent at 22 and 45 GHz. Two sources out of 30 remain undetected at our high sensitivities. The nuclear radio morphology is predominantly compact, sometimes accompanied by extended jet-like structures, or more complex features. The radio spectral energy distributions (SEDs) of the radio cores appear either as single or as a broken power law, a minority of them exhibit a peaked component. The spectral slopes are either flat/inverted or steep, up to a break/peak or over the whole range. The sample mean SED shows a flat slope up to 15 GHz that steepens between 15 and 22 GHz and becomes again flat above 22 GHz. Significant radio–X-ray correlations are observed at all frequencies. About half of the sample features extended emission, clearly resolved by the JVLA, indicating low-power jets or large-scale outflows. The unresolved cores, which often dominate the radio power, may be of jet, outflow, and/or coronal origin, depending on the observed frequency.

Key words: black hole physics – galaxies: active – galaxies: jets – galaxies: nuclei – galaxies: Seyfert – radio continuum: galaxies.

1 INTRODUCTION

The connection between the accretion and ejection physics in active galactic nuclei (AGN) has been one of the hot topics of extragalactic astrophysics since the first discoveries of active galaxies. The existence of scaling relations involving the black hole mass and fundamental quantities related to the host galaxy (e.g. Kormendy & Richstone 1995; Magorrian et al. 1998; Ferrarese & Merritt 2000; Gültekin et al. 2009) suggests that the AGN ejection activity and host galaxy evolution are entangled. Indeed, the mechanical kinetic energy ejected by the jet is believed to be one source of AGN feedback into the host galaxy (Morganti 2017). A connection between the accretion and the ejection phenomena, with analogous properties to AGN, has been observed in other accreting systems like black hole X-ray binaries (XRBs; e.g. Falcke, Körding & Markoff 2004), coronally active stars (e.g. Laor & Behar 2008; Raginski & Laor 2016), young stellar objects (e.g. Price, Pringle & King 2003; Ferreira & Deguiran 2013), cataclysmic variables (e.g. Körding et al. 2008), ultraluminous X-ray sources (e.g. Mezcua et al. 2013), and tidal disruption events (e.g. Zubovas 2019), suggesting a common underlying physics.

Historically, AGN has been divided between radio loud (RL) and radio quiet (RQ).[1] However, the radio-loudness definition strongly

★ E-mail: francesca.panessa@inaf.it (FP); gabriele.bruni@inaf.it (GB)

[1]The RL/RQ definition is based on the value of the ratio of optical-to-radio fluxes $R_O = \log \frac{f(4400\,\text{Å})}{f(6\,\text{cm})}$ (Kellermann et al. 1989). A similar definition has been proposed considering the radio-to-X-ray luminosities: $R_X = \log(L_R(6\,\text{cm})/L_{2-10\,\text{keV}})$, with −4.5 as dividing threshold between RQ and RL (e.g. Terashima & Wilson 2003; Panessa et al. 2006).

depends on the observed frequency, on the region size from where the radio flux is measured, and the boundaries between RL and RQ AGN may also depend on the accretion rate and luminosity of the source (Panessa et al. 2007). Padovani (2016) proposed a more physically meaningful dichotomy between 'jetted' and 'non-jetted' sources, where 'jetted' sources are those exhibiting a clear signature of a relativistic jet. In this work, we refer to RQ AGN in the sense of 'non-jetted' sources. There is emerging evidence that RQ AGN are not radio silent, as in these objects we do observe radio emission in a variety of shapes, scales, and strengths, with sources exhibiting outflowing and jet-like features, subrelativistic, less powerful, less collimated, and on smaller scales with respect to those of powerful RL AGN (e.g. Nagar et al. 2002); see Panessa et al. (2019) for a review.

Previous works focusing on the centimetre (cm) spectral range of the RQ population at arcsec resolution generally reported moderately to high detection fractions, i.e. 70–90 per cent (e.g. van der Hulst, Crane & Keel 1981; Kukula et al. 1995; Roy et al. 1998; Nagar et al. 1999; Thean et al. 2000). More recently, Smith et al. (2016, 2020) found a high detection fraction (∼96 per cent) for a sample of hard-X-ray-selected AGN from *Swift*/Burst Alert Telescope (BAT) at 22 GHz with a ∼1 arcsec resolution.

The morphology of the radio emission on arcsec scales is predominantly compact, either unresolved or marginally resolved. However, a number of sources exhibit extended structures, linear features, double/triple components, core plus jet-like features and diffuse emission, on spatial scales ranging from ∼kpc (e.g. Ulvestad, Wilson & Sramek 1981; Kukula et al. 1998; Leipski et al. 2006) down to few hundreds of pc (e.g. Kukula et al. 1995; Schmitt et al. 2001; Thean et al. 2001).

Previous studies of the spectral shape of RQ AGN were mainly performed at frequencies ≤15 GHz, usually adopting a two-frequency approach, which only gives a limited information on the overall shape due to the limited frequency coverage (e.g. Kellermann et al. 1989; Kukula et al. 1998; Chen et al. 2022). Only few works have adopted a multifrequency approach to study the spectral shape of RQ AGN, but still limited to the frequency range $\nu \leq 15$ GHz (e.g. Antonucci & Barvainis 1988; Barvainis, Lonsdale & Antonucci 1996; Kukula et al. 1998; Barvainis et al. 2005). These works have led to the finding that most sources show only steep spectra, however a number of them (roughly 40–50 per cent) exhibit flat/inverted spectra in the cm/sub-cm range (e.g. Antonucci & Barvainis 1988; Kukula et al. 1995, 1998; Barvainis et al. 1996, 2005; Chiaraluce et al. 2019; Laor, Baldi & Behar 2019).

In a number of sources the flat/inverted slope is found to dominate only at higher frequencies (≥few GHz), i.e. an excess emission is found with respect to the extrapolation from lower frequencies. This trend has been first reported as a 'high-frequency excess' up to 2 cm by Antonucci & Barvainis (1988) and Barvainis et al. (1996), and then as an mm-excess, up to ∼100 GHz, by Laor & Behar (2008) and Behar et al. (2015, 2018). Several radiative processes have been invoked to explain the evidence of flat/inverted cm/sub-cm spectra in RQ AGN, both thermal and non-thermal, like optically thick synchrotron emission from a compact source, either the base of the jet (e.g. Falcke, Malkan & Biermann 1995; Wilson & Colbert 1995; Baldi et al. 2021b, 2022) or a magnetically heated corona (e.g. Laor & Behar 2008; Raginski & Laor 2016), thermal free–free emission from nuclear sources at $T_B \sim 10^6$ and $\sim 10^4$ K emission from narrow-line region (NLR) or starburst (e.g. Antonucci & Barvainis 1988; Barvainis et al. 1996; Padovani et al. 2011; Condon et al. 2013).

The evidence of steep spectra in RQ AGN has been explained invoking synchrotron or free–free emission in the optically thin regime from disc or circumnuclear starburst regions, on host-galaxy scale but also down to few hundreds pc (e.g. Barvainis et al. 1996; Padovani et al. 2011; Condon et al. 2013; Zakamska et al. 2016); optically thin synchrotron from AGN-driven outflows, usually on few kpc scale (e.g. Mundell et al. 2000; Jiang et al. 2010; Zakamska & Greene 2014; Laor et al. 2019); or optically thin synchrotron emission from plasma blobs in a subrelativistic jet, usually associated with a linear morphology and on scales as small as hundreds of pc (e.g. Barvainis et al. 1996; Kukula et al. 1999; Laor et al. 2019).

As additional research channel, the study of correlations between the X-ray luminosity, considered a proxy for the accretion power, and the radio one, measuring the strength of ejection phenomena, has allowed to test different physical scenarios, such as radiatively efficient versus inefficient regimes (e.g. Merloni, Heinz & di Matteo 2003; Falcke et al. 2004; Coriat et al. 2011; Dong, Wu & Cao 2014; Dong & Wu 2015), or the so-called coronal models (e.g. Laor & Behar 2008; Raginski & Laor 2016).

This work is a completion of the results presented in Chiaraluce et al. (2020, hereafter Paper I). Here, we present the results from new Jansky Very Large Array (JVLA) multifrequency observations and spectral energy distributions (SEDs) for a sample of hard-X-ray-selected AGN, in a wide range of frequencies, 5–45 GHz, with a high sensitivity, few μJy beam^{-1}, and at a resolution of ∼ arcsec, i.e. spatial scales ≤kpc.

In this paper, we use the Λ cold dark matter (ΛCDM) with the following cosmological parameters: $H_0 = 67.4$ km s^{-1} Mpc^{-1}, $\Omega_m = 0.315$, and $\Omega_\Lambda = 0.685$ (Planck Collaboration VI 2020).

2 THE SAMPLE

The starting point of our project is the volume-limited sample of 89 hard-X-ray-selected AGN observed by the International Gamma-Ray Astrophysics Laboratory (*INTEGRAL*)/Imager on Board the *INTEGRAL* Satellite (IBIS) and presented in Malizia et al. (2009). We selected only the sources conveniently observable with the JVLA between 5 and 45 GHz, i.e. north of Dec. −30°, and we considered only Seyfert galaxies, criteria that reduce the sample to 44 objects (hereafter 'parent' sample). The characteristics of this sample have been extensively presented in Paper I, and are here briefly retrieved.

This hard-X-ray-selected sample has several advantages: (i) the hard-X-ray selection makes it relatively free of selection biases, e.g. absorption (see discussion in Ho & Ulvestad 2001 and Paper I); (ii) it comprises moderate-to-high-luminosity objects, with $41.5 \leq \log L_{2-10\,\mathrm{keV}}\,(\mathrm{erg\,s^{-1}}) \leq 44.5$; (iii) the accretion rates are relatively high: $-2.5 \leq \log L_{\mathrm{Bol}}/L_{\mathrm{Edd}} \leq -0.5$ (central panel of Fig. 1); (iv) it covers a wide range of radio luminosities (Fig. 2), with the bulk of the population made of RQ AGN (Fig. 3).

3 RADIO OBSERVATIONS AND DATA REDUCTION

In this work, we couple our high-frequencies radio data at 22 and 45 GHz (JVLA-C configuration, project 18B-163, ∼1 and 0.5 arcsec resolution, respectively) already published in Paper I, to lower frequencies (5, 10, and 15 GHz, i.e. C, X, and Ku bands, respectively) proprietary data obtained in JVLA-B configuration (project: 19A-018). The more extended configuration at lower frequencies guarantees us a matched resolution with high-frequencies data, a crucial point in order to build physically meaningful SEDs: at 5, 10, and 15 GHz the expected resolution is ∼1, 0.6, and 0.4 arcsec. Moreover, we complemented the high-frequency observations at 22 and 45 GHz with new ones obtained in the same configuration (project 20A-066).

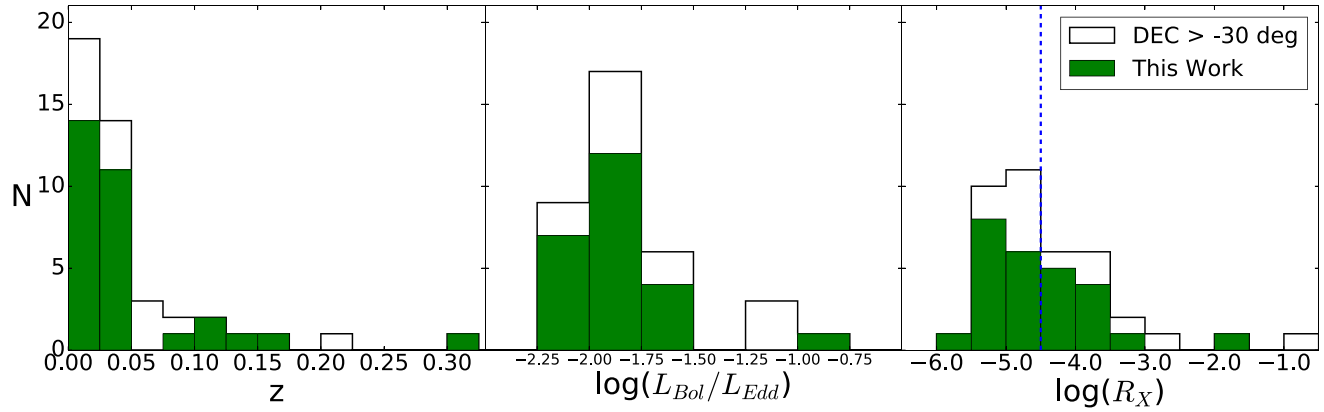

Figure 1. Histogram showing the distribution of redshift (from Malizia et al. 2009, left-hand panel). Eddington ratio ($L_{\rm Bol}/L_{\rm Edd}$, centre panel) and radio-loudness parameter (from quantities tabulated in Panessa et al. 2015, right-hand panel) for the parent sample (Dec. $> -30^{\circ}$, semifilled histogram) and for the sources considered in this work (green), i.e. having at least two SED data points. The blue, vertical dashed line is the $R_{\rm X} = -4.5$ limit of Terashima & Wilson (2003).

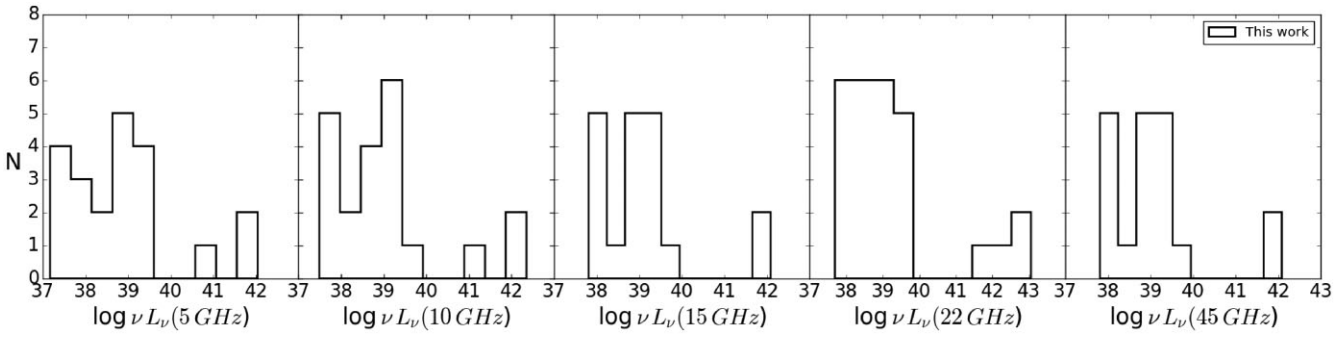

Figure 2. Histogram showing the distribution of core radio luminosities $\log \nu L_\nu$ at the different frequencies for sources in the sample.

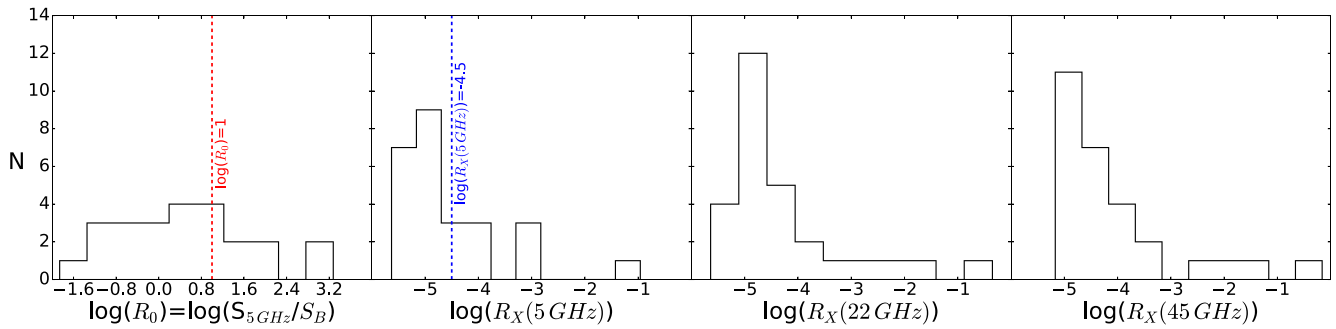

Figure 3. Histogram showing the distribution of radio loudness for the sources in the sample based on different definitions, i.e. Kellermann et al. (1989) (first panel, from left, 9/30 classify as RL); Terashima & Wilson (2003) at 5 GHz (second panel, 10/30 classify as RL), 22 GHz (third panel), and at 45 GHz (fourth panel). The vertical lines denote the RQ/RL limit depending on the definition.

Finally, we searched in the Very Large Array (VLA) archive low-frequency data for the objects for which our own proprietary data were not available (i.e. NGC 788, NGC 1068, QSO B0241+62, NGC 1142, B3 0309+411B, MCG +08-11-11, Mrk 3, and Mrk 6). When available, we selected observations in the same configurations (VLA-B), when not we considered other available configurations (mostly A), and in order to match the resolution a tapering has been applied (see next section).

The above strategy translates into 30 objects out of 44 with at least two SED data points. In Table 1, we summarize the characteristics of the sample together with information on the observations and the corresponding projects: nine sources have only two SED data points; one source (Mrk 50) has three SED data points; two sources have four data points (NGC 788 and B3 0309+411B), the majority of sources (18 out of 30) have five SED data points.

In Fig. 1, we plot a histogram of the distribution of the relevant physical quantities of sources in this work, i.e. redshift, Eddington ratio, and X-ray radio loudness ($R_{\rm X} = \log(L_{\rm R}(6\,{\rm cm})/L_{2-10\,{\rm keV}})$), as compared to the whole sample of 44 source north Dec. $\geq -30^{\circ}$. A Kolmogorov–Smirnov test comparing the two distributions results, in all cases, in a $P \sim 0.99$, so the null hypothesis that the two samples are drawn from the same parent population cannot be rejected. This would suggest that the physical conclusions that can be drawn from

Table 1. List of sources together with observations information. Column (1): target name; columns (2) and (3): right ascension and declination (J2000) from Malizia et al. (2009); column (4): Seyfert type; column (5): redshift; columns (6), (7), (8), (9), and (10): C, X, Ku, K, and Q band projects, respectively. For the archival data we use the following notation: VLA project (month/year) [VLA configuration].

					Observations				
Target	RA (J2000)	Dec. (J2000)	Seyfert type	z	C (5 GHz)	X (10 GHz)	Ku (15 GHz)	K (22 GHz)	Q (45 GHz)
(1)	(2)	(3)	(4)	(5)	(6)	(7)	(8)	(9)	(10)
IGR J00333+6122	00:33:18.41	+61.27.43.10	S1.5	0.105	···	···	···	18B-163	18B-163
NGC 788	02:01:06.40	−06:48:56.0	S2	0.0136	AW0126 (02/85) [A]	AM384(12/92)[A]	···	18B-163	18B-163
NGC 1068	02:42:40.71	−00:00:47.8	S2	0.0038	BG066 (04/99) [B]	AZ0053(04/92)[C]	AW0085(01/84)[B]	18B-163	18B-163
QSO B0241+62	02:44:40.71	+62.28.06.5	S1	0.044	AM0124 (06/86) [B/A]	AS644(11/98)[C]	AS0786(04/04)[C]	18B-163	18B-163
NGC 1142	02:55:12.19	−00.11.02.3	S2	0.0288	12A-066 (06/12) [B]	AP233(06/91)[A] AP212(04/92)[B]	AJ105(05/84)[B]	18B-163	18B-163
B3 0309+411B	03:13:01.96	+41.20.01.2	S1	0.136	BT0007 (05/94) [A/B]	BM0074(04/97)[B]	···	18B-163	18B-163
NGC 1275	03:19:48.16	+41.30.42.1	S2	0.0175	···	···	···	18B-163	18B-163
LEDA 168563	04:52::04.85	+49.32.43.7	S1	0.029	···	···	···	18B-163	18B-163
4U 0517+17	05:10:45.51	+16.29.55.8	S1.5	0.0179	···	···	···	18B-163	18B-163
MCG +08-11-11	05:54:53.61	+46.26.21.6	S1.5	0.0205	ULVE (03/82) [A]	AB0973(11/04)[A]	AU0018(11/83)[A]	18B-163	18B-163
Mrk 3	06:15:36.36	+71.02.15.1	S2	0.0135	AW0258 (08/90) [A] GK0011 (02/94) [B]	AW0278(09/91)[A] BM0124(06/00)[B]	AP0142(09/87)[A]	18B-163	18B-163
Mrk 6	06:52:12.25	+74.25.37.5	S1.5	0.0188	AB0740 (07/95) [A] AB0740 (11/95) [B] AB0740 (05/95) [D]	AW0278(09/91)[A]	AP0142(10/87)[A]	18B-163	18B-163
NGC 4151	12:10:32.58	+39:24:20.6	S1.5	0.0033	···	···	···	18B-163	18B-163
Mrk 50	12:23:24.14	+02.40.44.8	S1	0.0234	19A-018	19A-018	19A-018	···	···
NGC 4388	12:25:46.75	+12.39.43.5	S2	0.0084	19A-018	19A-018	19A-018	18B-163	18B-163
LEDA 170194	12:39:06.32	−16.10.47.8	S2	0.036	19A-018	19A-018	19A-018	20A-066	20A-066
NGC 4593	12:39:39.42	−05.20.39.3	S1	0.009	19A-018	19A-018	19A-018	20A-066	20A-066
IGR J13091+1137	13:09:05.60	+11.38.02.9	S2	0.0251	19A-018	19A-018	19A-018	20A-066	20A-066
NGC 5252	13:38:16.00	+04.32.32.5	S2	0.023	19A-018	19A-018	19A-018	18B-163	18B-163
NGC 5506	14:13:14.87	−03.12.26.9	S1.9	0.0062	19A-018	19A-018	19A-018	20A-066	20A-066
IGR J16385−2057	16:38:30.91	−20.55.24.6	NLS1	0.0269	···	···	···	20A-066	20A-066
IGR J16426+6536	16:43:04.70	+65:32:50.9	NLS1	0.323	···	···	···	18B-163 20A-066	18B-163 20A-066
IGR J17513−2011	17:51:13.62	−20.12.14.6	S1.9	0.047	19A-018	19A-018	19A-018	20A-066	20A-066
IGR J18027−1455	18:02:45.50	−14.54.32.0	S1	0.035	···	···	···	20A-066	20A-066
IGR J18259−0706	18:25:57.58	+07.10.22.8	S1	0.037	19A-018	19A-018	19A-018	20A-066	20A-066
2E 1853.7+1534	18:56:01.28	+15.38.05.7	S1	0.084	···	···	···	20A-066	20A-066
IGR J20186+4043	20:18:38.73	+40.40.59.9	S2	0.0144	19A-018	19A-018	19A-018	20A-066	20A-066
4C +74.26	20:42:37.30	+75.08.02.4	S1	0.104	19A-018	19A-018	19A-018	20A-066	20A-066
IGR J23308+7120	23:30:37.28	+71.22.46.0	S2	0.037	19A-018	19A-018	19A-018	20A-066	20A-066
IGR J23524+5842	23:52:22.11	+58.45.30.7	S2	0.164	19A-018	19A-018	19A-018	20A-066	20A-066

the sources considered in this work are likely representative of the whole sample.

The project 19A-018 has been observed in the period 2019 February–May and the project 20A-066 in the period 2020 February–May. The characteristics of observations for the high-frequency project 20A-066 are the same of 18B-163, presented in section 3 of Paper I, and we refer to that section for the details. Sources in 19A-018 were observed at 5, 10, and 15 GHz for a minimum of 1 min to a maximum of 5 min. We applied phase calibration, bracketing targets with suitable sources within a radius of 10°. The scans of the absolute flux density scale calibrator has been performed once per scheduling block, typically at the beginning or end of it, and, at a given frequency, it is observed for no less than 2 min and 30 s.

The data calibration and reduction procedure for the proprietary JVLA data has been performed with the calibration pipeline within the Common Astronomy Software Application (CASA 5.4.1 version;[2] McMullin et al. 2007). After calibration, the plots were inspected for residual radio frequency interference (RFI). For the image reconstruction, the TCLEAN task in CASA has been used, applying the Högbom (1974) deconvolver. We produced full resolution maps considering as initial weighting the Briggs (1995) one with robustness parameter equal to 0.5, which ensures a balance between resolution and sensitivity. However, in order to have X and Ku maps at a matched resolution with respect to C band, we produced naturally weighted tapered maps, in order to give more weight to the short baselines and have an approximately equal ultraviolet (UV) coverage.

The typical rms achieved is ∼10–40 arcsec, in agreement with proprietary post-upgrade JVLA data (see Table 3 in Supplementary Material). For the archival VLA data, the reduction has been performed with the Astronomical Image Processing System (AIPS) in the 31DEC20 version,[3] following standard procedures. The imaging procedure has been conducted via the task IMAGR. In all cases, self-calibration has been performed for all the sources strong enough to provide enough flux density for the model.

For both the proprietary JVLA data and the archival VLA ones, the image analysis has been performed via the CASA task IMFIT. Based on the source morphology, single/multiple Gaussian fit on the image plane has been performed. A comparison of the flux densities of calibrators for the proprietary JVLA data with tabulated values in Perley & Butler (2017) led to the estimation of a ∼5 per cent error in the flux calibration; for the archival data a more conservative 10 per cent has been adopted. The uncertainties in the final flux density measurements are affected by fitting errors from IMFIT, and flux calibration error, which are added in quadrature and adopted as the error measurements. In the case of components with a resolved morphology, the error associated with the flux determination is given by the formula $\sigma_S = \sqrt{N \times (\mathrm{rms})^2 + (A_s \times S)^2}$, where N is the number of beam areas covered by a source of flux density S, and A_s takes into account the uncertainty in the absolute flux density scale (0.05–0.1; see Ho & Ulvestad 2001).

In Table 1, we report the source coordinates taken from Malizia et al. (2009). In a number of sources the above positions display a significant offset from the derived radio ones (the latter reported in Table 3 in Supplementary Material). For this reason, we performed a careful cross-check with all available positions (from optical, X-ray, infrared, etc., observations) in literature[4] for each source, in order to determine the likely core component. In the maps, the white (or black) crosses represent the original optical coordinates as in Malizia et al. (2009), as quoted in Table 1, that were adopted during the scheduling of our observations and therefore are their phase centres. In Table 2, in Supplementary Material we report the integrated and peak radio luminosities of the core component at all frequencies, and in Table 3 in Supplementary Material we report the derived parameters from the imaging analysis. The complete set of maps for the entire sample is available on the project's website,[5] while a representative image for each source, together with its SED, is reported in Fig. 2 in Supplementary Material. In Table 2, we report the X-ray (2–10 keV and 10–100 keV) and bolometric luminosities and the corresponding Eddington ratios (as detailed in Paper I). The optical radio-loudness parameter (Kellermann et al. 1989) and the X-ray radio-loudness parameter (Terashima & Wilson 2003) are calculated using the radio luminosities at 5, 22, and 45 GHz.

4 RESULTS

4.1 Detection rates, radio luminosities, and radio loudness

We find high detection rates of radio emission at all frequencies, with detection fractions that decrease with frequency, i.e. 21/21, 21/21, 19/19, 26/29, and 24/29 at 5, 10, 15, 22, and 45 GHz, respectively, which translate into rates of 96 ± 8, 96 ± 8, 95 ± 8, 87 ± 12, and 81 ± 14, respectively.[6]

In Fig. 2, we show the distribution of core radio luminosities for the sources in the sample at different frequencies. The bulk of sources has core radio luminosities in the range $37 \leq \log \nu L_\nu\,(\mathrm{erg\,s^{-1}}) \leq 40$, well below the values observed in radio galaxies (i.e. $\log \nu L_\nu\,(\mathrm{erg\,s^{-1}}) > 42$; Zirbel & Baum 1995).

In Fig. 3, we show the distribution of radio-loudness parameters of the core component at different frequencies. The fraction of radio sources that can be classified as RL is 30 and 33 per cent considering the classical radio-loudness parameter and the X-ray one at 5 GHz, respectively (Terashima & Wilson 2003). However, given the low radio luminosities and the caveats associated with the definition of a boundary in the radio-loudness parameter, we consider as RQ AGN the majority of the sources in our sample, except for the three most powerful radio emitters already mentioned in Paper I, i.e. QSO B0241+62, B3 0309+411B, and NGC 1275, and the giant radio galaxy 4C +74.26 (e.g. Bruni et al. 2020, and references therein), resulting in ∼13 per cent of RL AGN in the sample. This fraction of RL AGN is consistent with what already observed so far in hard-X-ray-selected samples (e.g. Bassani et al. 2016, and references therein).

4.2 Undetected sources

Two sources out of 30 were not detected by our observations, i.e. IGR J16426+6536 and IGR J18027−1455, and for both only observations at 22 and 45 GHz were available. For both we give 3σ upper limits of ∼0.1 and ∼0.15 mJy beam^{-1} at 22 and 45 GHz, respectively, which result, in the case of IGR J18027−1455, in upper limits on the radio luminosities of $\log L_\mathrm{R}\,(\mathrm{erg\,s^{-1}}) \sim 37.8$ and 38.3

[2] https://casa.nrao.edu
[3] http://www.aips.nrao.edu
[4] With the NASA/IPAC Extragalactic Database (NED) and SIMBAD data bases.

[5] https://sites.google.com/inaf.it/hxagn/radio-images
[6] Because of the limited statistics of the sample, in order to estimate the detection fractions and associated uncertainties, we used the Laplace point estimate formula (Laplace 1812) and the Adjusted Wald Method (e.g. Sauro & Lewis 2005).

Table 2. Luminosities and radio-loudness parameters: Column (1): target name; column (2): 2–10 keV X-ray luminosity from Malizia et al. (2009); column (3): 20–100 keV X-ray luminosity from Malizia et al. (2009); column (4): bolometric luminosity; column (5): Eddington ratio; column (6): optical radio-loudness parameter (Kellermann et al. 1989); column (7): X-ray radio loudness at 5 GHz; column (8): X-ray radio loudness at 22 GHz; column (9): X-ray radio loudness at 45 GHz.

Name	$\log(L_{2-10\,\mathrm{keV}})$ (erg s^{-1})	$\log(L_{20-100\,\mathrm{keV}})$ (erg s^{-1})	$\log(L_{\mathrm{Bol}})$ (erg s^{-1})	$\log(L_{\mathrm{Bol}}/L_{\mathrm{Edd}})$	$\log(R_{\mathrm{O}})$	$\log(R_{\mathrm{X}}^{5\,\mathrm{GHz}})$	$\log(R_{\mathrm{X}}^{22\,\mathrm{GHz}})$	$\log(R_{\mathrm{X}}^{45\,\mathrm{GHz}})$
(1)	(2)	(3)	(4)	(5)	(6)	(7)	(8)	(9)
IGR J00333+6122	44.19	44.44	44.80	−1.84	1.90	−4.42	−4.64	−4.71
NGC 788	42.86	43.29	43.55	−2.06	−1.04	−5.42	−5.01	−4.9
NGC 1068	42.95	43.35	43.36	−1.95	0.04	−3.92	−4.11	−4.06
QSO B0241+62	43.87	44.41	44.39	−1.80	0.70	−3.06	−1.91	−1.60
NGC 1142	43.82	43.96	45.23	−2.27	0.08	−5.25	−4.88	−4.76
B3 0309+411B	45.04	44.99	...	...	3.28	−3.00	−1.96	−1.67
NGC 1275	42.89	43.38	44.32	−2.28	2.99	−0.96	−0.35	−0.16
LEDA 168563	43.9	44.04	44.33	−1.77	1.50	−4.70	−4.80	−4.80
4U 0517+17	43.23	43.62	43.44	−1.66	...	−5.27	−4.75	−4.40
MCG +08-11-11	43.69	43.74	43.90	−1.65	1.27	−4.25	−4.29	−3.98
Mrk 3	44.17	43.79	44.77	−2.03	1.03	−4.79	−5.03	−4.98
Mrk 6	43.27	43.57	44.27	−1.96	1.17	−3.93	−3.40	−3.31
NGC 4151	43.05	43.16	43.89	−1.91	0.60	−5.41	−4.84	−4.73
Mrk 50	43.05	43.2	43.66	−1.84	−1.02	−5.53	...	...
NGC 4388	43	43.54	43.16	−1.80	−0.80	−4.94	−5.05	−4.83
LEDA 170194	43.48	44.22	44.76	−2.24	0.30	−4.42	−3.67	−3.20
NGC 4593	42.8	43.09	43.12	−1.72	−1.86	−5.63	−4.95	−4.49
IGR J13091+1137	43.44	43.77	44.44	−2.16	−0.90	−5.49	−5.17	−5.08
NGC 5252	43.72	43.71	44.89	−2.21	0.60	−4.71	−4.39	−4.60
NGC 5506	42.83	42.85	42.96	−1.79	0.90	−3.91	−3.85	−3.77
IGR J16385−2057	43.02	43.39	43.26	−1.67	...	...	−4.37	−4.32
IGR J16426+6536	...	45.97	...	...	...	...	...	...
IGR J17513−2011	43.4	44.1	43.09	−1.01	...	−4.75	−4.29	−3.89
IGR J18027−1455	43.23	44.04	43.83	−1.83	...	...	<−5.46	<−4.97
IGR J18259−0706	43.19	43.66	...	...	...	−4.99	−4.65	−4.37
2E 1853.7+1534	44.25	44.56	44.55	−1.70	...	...	−5.64	<−5.17
IGR J20186+4043	42.57	42.98	...	...	−0.67	−4.72	−4.62	−4.60
4C +74.26	44.75	45.04	45.76	−1.96	1.92	−3.20	−2.54	−2.45
IGR J23308+7120	42.8	43.55	...	...	−0.44	−5.16	<−5.11	<−4.28
IGR J23524+5842	44.41	44.85	...	...	1.12	−5.04	−5.22	<−4.67

(upper limits on the radio powers of $L_\nu\,(\mathrm{W\,Hz^{-1}}) \sim 3 \times 10^{20}$ and $L_\nu\,(\mathrm{W\,Hz^{-1}}) \sim 4.5 \times 10^{20}$ at 22 and 45 GHz, respectively). The derived upper limits on the X-ray radio-loudness parameter are of −5.4 and −4.9 at the two frequencies, respectively, placing these sources at the very-low-power end of the radio-loudness distribution. The source IGR J16426+6536 benefits from observations in two epochs, one in 2018 November and presented in Paper I, and one in 2020 June, presented here. In both cases the source is undetected at a similar flux limit (see Table 3 in Supplementary Material), variability at 17 months scales can therefore be ruled out. Deeper observations, achievable with longer integration times, would be required to confirm the radio-silent nature of these sources.

4.3 Morphology

We divided the morphology of the sources in the sample into four main classes, adapting the classification in Baldi et al. (2021a), considering both full array and tapered radio maps. In Table 3, we report the morphological classification (column 2) for each source and in Fig. 4, we report an examples of each of the four morphological classes.

(i) *Core or core + jet/lobe (A)*. Sources with a single core component, either resolved or marginally resolved, sometimes with a small-scale protrusion (either one-sided or two-sided); 17/30 sources belong to this class (e.g. IGR J17513−2011).

(ii) *One-sided jet (B)*. Sources with an extended asymmetric jet, which is possibly resolved into several emitting components at higher resolutions; 7/30 sources are in this class (e.g. IGR J23524+5842).

(iii) *Triple (C)*. Sources exhibiting a triple morphology, interpreted as the radio core plus symmetric jet/lobes (one source: LEDA 170194).

(iv) *Jet + complex (D)*. Sources with a complex structure, with multiple components, either compact, diffuse, and/or extended; three sources fall in this classification, i.e. NGC 1068, NGC 1142, and NGC 5506. Note that the D classification corresponds to the E classification in Baldi et al. (2021a).

The morphological study for the sources across the cm-wave range reveals a prevalence of compact components, either unresolved or marginally resolved, with nearly a half of the sample sources exhibiting jet-like structures, as well as triple and more complex ones that extend up to kpc scales. We note that the morphological classification depends on the distance of the source, i.e. for high z sources structures below the kpc scales are not resolved. However the majority of the sample sources are located in the nearby Universe, allowing us to map projected linear sizes of hundreds of pc (e.g. the nearest source is NGC 4593, ∼190 pc). On the other hand, high-z objects ($z > 0.1$) in our sample are mostly radio galaxies (e.g.

Table 3. The two-frequency spectral indices (and associated uncertainties) for the sources and the multiple components, when present. The frequency pairs considered are 5–10 GHz, 10–15 GHz, 15–22 GHz, 22–45 GHz; for NGC 788 and B3 0309+411B we report the 10–22 GHz spectral index, due to the lack of 15 GHz data. We also indicate the morphological classification based on the four classes.

Name	Radio morph	Component	α_{5-10}	α_{10-15}	α_{15-22}	α_{22-45}	α_{10-22}
IGR J00333+6122	A	Core	···			1.2 ± 0.4	
NGC 788	A	Core	0.8 ± 0.2	···	···	0.4 ± 0.3	-0.05 ± 0.20
NGC 1068		a	0.65 ± 0.13	1.64 ± 0.13	0.69 ± 0.17	0.9 ± 0.1	
	D	b(Core)	0.49 ± 0.13	1.59 ± 0.13	1.1 ± 0.2	0.8 ± 0.1	
		d	···	···	0.62 ± 0.18	0.47 ± 0.01	
		SW	···	···	-0.24 ± 0.19	0.14 ± 0.10	
QSO B0241+62	B	Core	-0.86 ± 0.13	-1.34 ± 0.12	0.252 ± 0.180	0.3 ± 0.1	
		Blob	0.57 ± 0.13	2.4 ± 0.2	···	···	
NGC 1142	D	East	···	···	···	···	
		A1	2.45 ± 0.18	-0.18 ± 0.18	1.28 ± 0.25	0.9 ± 0.3	
		A2	1.72 ± 0.17	-0.24 ± 0.16	1.83 ± 0.23	1.4 ± 0.1	
		b(Core)	0.04 ± 0.17	-0.17 ± 0.15	1.26 ± 0.21	0.5 ± 0.1	
		d	1.11 ± 0.18	1.03 ± 0.12	0.73 ± 0.22	···	
B3 0309+411B	B	Core	-0.38 ± 0.13	···	···	0.06 ± 0.10	-0.7 ± 0.1
		NW	0.11 ± 0.13	···	···	···	
NGC 1275	A	Core	···	···	···	0.4 ± 0.1	
LEDA 168563	A	Core	···	···	···	1.07 ± 0.12	
4U 0517+17	A	Core	···	···	···	-0.09 ± 0.11	
MCG +08-11-11	B/C	Core	1.07 ± 0.13	1.1 ± 0.1	0.14 ± 0.19	0.7 ± 0.1	
		Jet	2.23 ± 0.13	2.5 ± 0.5	-3.2 ± 0.9	1.1 ± 0.4	
Mrk 3		West	1.31 ± 0.13	0.77 ± 0.12	1.8 ± 0.3	1.2 ± 0.1	
	B	East(core)	1.41 ± 0.13	0.35 ± 0.10	1.3 ± 0.1	0.87 ± 0.09	
Mrk 6		N	0.98 ± 0.07	1.13 ± 0.10	···	···	
	B/C/D	S(core)	0.91 ± 0.07	1.0 ± 0.1	···	···	
		Ext-EW	2.6 ± 0.1	···	···	···	
NGC 4151	A	Core	···	···	···	0.7 ± 0.1	
Mrk 50	A	Core	-0.06 ± 0.20	0.03 ± 0.23	···	···	
NGC 4388	B(core)	NE	0.9 ± 0.1	0.8 ± 0.2	1.08 ± 0.20	0.27 ± 0.11	
		SW	0.8 ± 0.1	0.47 ± 0.18	1.45 ± 0.22	1.6 ± 0.3	
		North	1.11 ± 0.13	5.4 ± 0.1	···	···	
LEDA 170194	C	Core	-0.09 ± 0.14	0.42 ± 0.17	-0.21 ± 0.14	-0.8 ± 0.4	
		SW	0.14 ± 0.24	1.9 ± 0.4	···	···	
		NE	0.7 ± 0.5	2.0 ± 0.9	···	···	
NGC 4593	A	Core	-1.01 ± 0.15	-0.23 ± 0.16	0.77 ± 0.18	-0.54 ± 0.12	
IGR J13091+1137	A	Core	-0.57 ± 0.16	-0.51 ± 0.19	2.6 ± 0.2	0.7 ± 0.4	
NGC 5252	A	Core	0.04 ± 0.11	0.61 ± 0.17	0.28 ± 0.20	1.7 ± 0.1	
NGC 5506	D	Core	0.95 ± 0.15	0.78 ± 0.11	1.1 ± 0.2	0.76 ± 0.11	
IGR J16385−2057	A	Core	···	···	···	0.74 ± 0.25	
IGR J17513−2011	A	Core	-0.004 ± 0.140	-0.13 ± 0.18	0.9 ± 0.2	-0.40 ± 0.14	
IGR J18259−0706	A	Core	0.86 ± 0.14	0.8 ± 0.2	-0.6 ± 0.4	0.07 ± 0.30	
2E 1853.7+1534	A	Core	···	···	···	···	
IGR J20186+4043	A	Core	0.87 ± 0.14	0.44 ± 0.17	1.3 ± 0.2	0.9 ± 0.3	
4C +74.26	A	Core	-0.15 ± 0.09	0.003 ± 0.200	0.24 ± 0.20	0.7 ± 0.1	
IGR J23308+7120	A	Core	0.64 ± 0.30	-0.4 ± 0.4	···	···	
IGR J23524+5842	B	Core	-0.6 ± 0.2	0.65 ± 0.20	4.63 ± 0.34	···	
		NE	1.33 ± 0.40	1.8 ± 0.7	···	···	

3C +74.26, ∼2 kpc) with a known morphology. The classification also depends on the selected frequency. As an example, MCG +08-11-11 appears as a core plus a one sided jet-like feature in our maps at matched resolution of ∼1 arcsec, however, in the full resolution image, the core is resolved into three components, the central one being the core (e.g. Ulvestad & Wilson 1986). Indeed, sources with extended emission are best detected at low frequencies for a combination of effects. The surface brightness is enhanced by the steep spectrum and for a given JVLA configuration, the beam is larger, increasing the sensitivity to low surface brightness emission.

4.4 Radio spectral energy distributions

With the present observations, spanning the 5–45 GHz interval, we can build spectral energy distributions (SEDs) in the cm/sub-cm range at a matched resolution (∼arcsec) and sensitivity (a few μJy beam^{-1}) for a statistically relevant sample. In this way it is possible to characterize the wide-frequency emission for the emitting components, both nuclear and extranuclear, and interpret them in light of models invoked for emission in RQ objects.

The definition of the spectral index used in this work is $S_\nu^{\rm I} \propto \nu^{-\alpha}$, where $S_\nu^{\rm I}$ is the integrated flux density. The uncertainties associated with the spectral indices have been estimated as

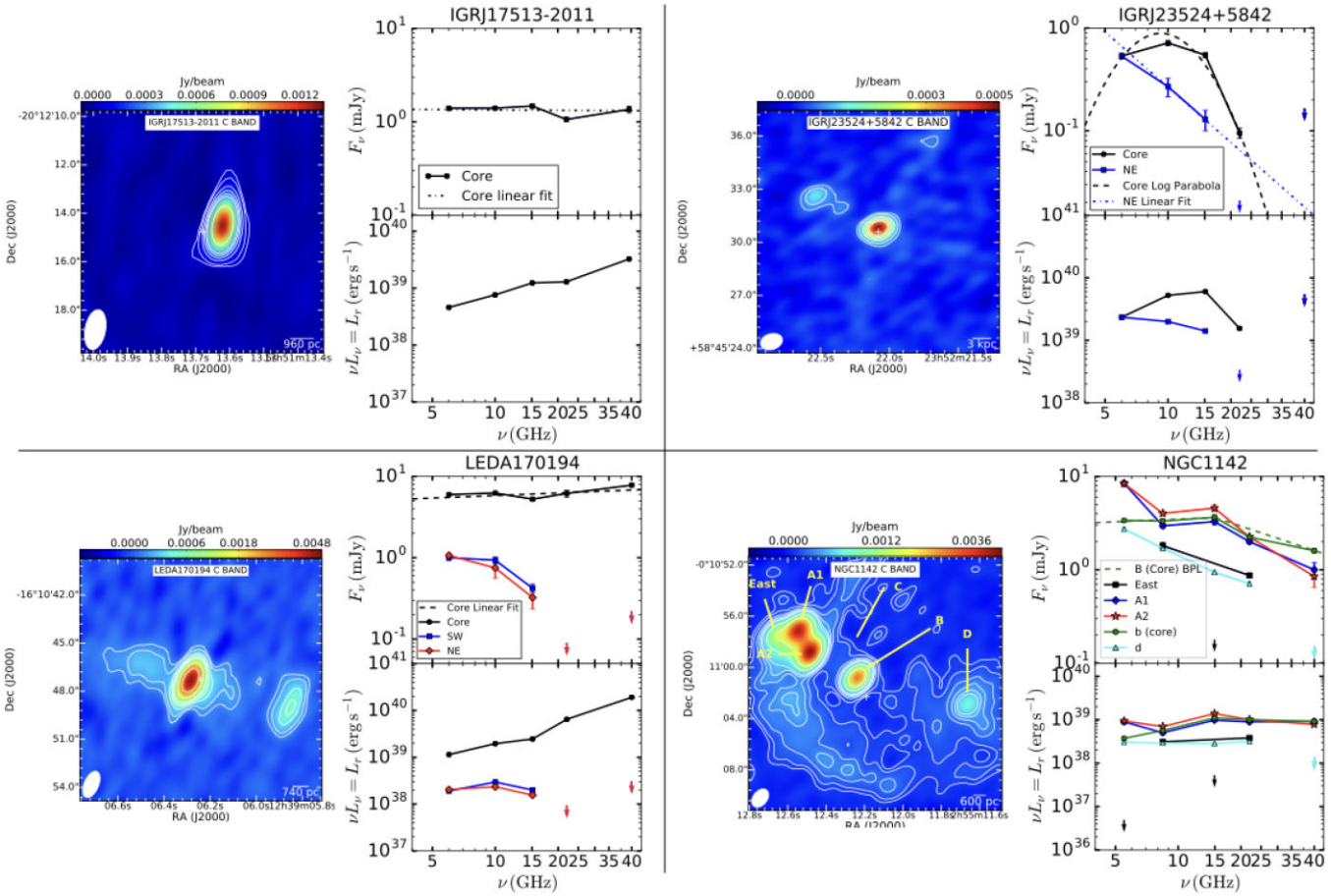

Figure 4. Radio maps of sources considered as an example for the four morphological types adopted in Section 4.3: top-left, IGR J17513−2011 (morphological class A); top-right, IGR J23524+5842 (morphological class B); bottom-left, LEDA 170194 (morphological class C); bottom-right, NGC 1142 (morphological class D). For space reasons, only the 5 GHz (C band) maps are shown. For each source we also show the corresponding SED, in which we indicate the core and all the other emitting components (if present). The SED and morphology for the remaining sources are shown in Fig. 2 in Supplementary Material.

$\sqrt{(\sigma_{f_1}/S_{f_1})^2 + (\sigma_{f_2}/S_{f_2})^2}/\ln(f_2/f_1)$, where $\sigma_{f_{1,2}}$ and $S_{f_{1,2}}$ are the uncertainties on the flux density and the flux density at the two frequencies (Ho & Ulvestad 2001), which are the central frequencies of the K and Q bands (therefore the flux densities are the mean across the bandwidth). We define a steep spectrum as having $\alpha \geq 0.5$, and a flat one as having $\alpha < 0.5$, as in Panessa & Giroletti (2013). We define a spectrum as inverted if $\alpha < 0$.

In order to characterize the spectral shape of the core components, we adopted the classification presented in Barvainis et al. (1996), (see also Scheuer & Williams 1968), i.e. single power-law (S) spectra, for which a simple power-law fit is sufficient, concave (C+) and convex (C−) spectra, for which the spectrum can be fitted by a quadratic polynomial, and complex spectra (CPX), which do not fit in any of the above cases. Based on the evidence in the sample, we add an extra class, the spectra for which a broken power-law (BPL) fit represents well the data.

In Table 4, we report the results of the SED fitting, first for the BPL sources, then for the convex sources, and finally for the single power-law ones. In Fig. 2 in Supplementary Material, we show the spectral flux and energy distributions of sources across the frequency range covered by our observations (sources are ordered as in Table 4), while in Fig. 5, we show the distribution of two-frequency spectral indices for the core components of sources in the sample for the frequency pairs 5–10, 10–15, 15–22, and 22–45 GHz. The relative fraction of sources in the different classes are the following: 67 per cent of single power-law spectra (e.g. left-hand panels of Fig. 4), 14 per cent of convex spectra (e.g. top right-hand panel of Fig. 4), 19 per cent of BPL spectra (e.g. bottom left-hand panel of Fig. 4), neither of concave nor complex spectra. However, cases that have been classified as convex, i.e. NGC 4593 and IGR J13091+1137, could be classified in the complex class as well (see next sections). In this classification we excluded the sources with less than two frequency points (6/30 with two data points, 1/30 with one, and 2/30 undetected).

The extranuclear components, when present, generally exhibit steep spectra.

5 DISCUSSION

5.1 Detection rates of radio emission

The detection rates of radio emission we find here are generally higher with respect to values reported in literature for surveys of Seyfert galaxies, especially at lower frequencies, typical percentages 70–90 (e.g. van der Hulst et al. 1981; Antonucci & Barvainis 1988; Kellermann et al. 1989; Ulvestad & Wilson 1989; Kukula et al. 1995; Roy et al. 1998; Nagar et al. 1999; Thean et al. 2000; Nyland et al. 2020; Sebastian et al. 2020; Silpa et al. 2020; Smith et al. 2020; Baldi et al. 2021a). However, a comparison with these works is not

Table 4. Results of the SED fitting for the sources in the sample. Column (1): target name; column (2): component; column (3): classification of core SED; column (4): spectral index from linear fit to all points; column (5): break frequency (in GHz) in case of broken power-law (BPL) fit or peak in case of log-parabola fit; column (6): spectral index at $\nu \leq \nu_{\rm B}$ (before break or peak); column (7): spectral index at $\nu \geq \nu_{\rm B}$ (after break or peak). We show first the sources for which the core can be fitted by a BPL, then those for which we performed a log-parabolic fit, finally the sources for which the core can be fitted by a single power law. The sources for which only two data points or less were available (6/30) are omitted.

Target (1)	Comp (2)	SED class (3)	$\alpha_{\rm All}$ (4)	$\nu_{\rm Break/Peak}$ (5)	$\alpha(\nu \leq \nu_{\rm Break/Peak})$ (6)	$\alpha(\nu \geq \nu_{\rm Break/Peak})$ (7)
NGC 5252	Core	BPL	–	∼10	-0.04 ± 0.11	$+0.56 \pm 0.12$
IGR J18259−0706	Core	BPL	–	∼15	0.77 ± 0.03	0.03 ± 0.09
QSO B0241+62	Core	BPL	–	∼15	-1.12 ± 0.15	0.31 ± 0.03
	Blob	–	–	∼10	0.57 ± 0.13	2.4 ± 0.2
NGC 1142	d	–	$+0.97 \pm 0.04$	–	–	–
	East	–	$+0.76 \pm 0.09$	–	–	–
	A1	–	$+0.94 \pm 0.11$	–	–	–
	A2	–	$+1.25 \pm 0.25$	–	–	–
	b (Core)	BPL	–	∼15	-0.09 ± 0.05	$+0.74 \pm 0.11$
NGC 4593	Core	C–	–	∼15	-1.01 ± 0.15	$+0.8 \pm 0.2$
	Excess	–	-0.54 ± 0.12	–	–	–
IGR J13091+1137	Core	C–	–	∼10	-0.57 ± 0.16	$+2.6 \pm 0.2$
	Excess	–	$+0.7 \pm 0.4$	–	–	–
IGR J23524+5842	Core	C–	–	∼9	-0.57 ± 0.17	$+4.6 \pm 0.3$
	North	–	1.78 ± 0.02	–	–	–
Mrk 50	Core	S	-0.02 ± 0.02	–	–	–
NGC 5506	Core	S	$+0.85 \pm 0.02$	–	–	–
IGR J17513−2011	Core	S	$+0.01 \pm 0.08$	–	–	–
IGR J20186+4043	Core	S	$+0.90 \pm 0.03$	–	–	–
MGC +08-11-11	Core	S	$+0.78 \pm 0.09$	–	–	–
	Jet	–	–	–	–	–
LEDA 170194	Core	S	-0.10 ± 0.08	–	–	–
	SW	–		∼10	$+0.14 \pm 0.24$	1.9 ± 0.4
	NE	–		∼10	0.7 ± 0.5	2.0 ± 0.9
Mrk 3	West	S	1.22 ± 0.07	–	–	–
	East (core)	–	0.88 ± 0.06	–	–	–
Mrk 6	North	–	$+1.24 \pm 0.05$	–	–	–
	South (core)	S	$+0.92 \pm 0.04$	–	–	–
NGC 1068	d	–	$+0.81 \pm 0.16$	–	–	–
	a	–	$+1.00 \pm 0.08$	–	–	–
	b (Core)	S	$+1.04 \pm 0.09$	–	–	–
	SW	–	–	–	–	–
NGC 788	Core	S	$+0.19 \pm 0.06$	–	–	–
4C +74.26	Core	S	$+0.23 \pm 0.13$	–	–	–
B3 0309+411B	Core	S	-0.4 ± 0.1	–	–	–
IGR J23308+7120	Core	S	$+0.21 \pm 0.30$	–	–	–
NGC 4388	NE (core)	S	0.67 ± 0.09	–	–	–
	SW	–	–	∼15	$+0.68 \pm 0.08$	$+1.53 \pm 0.01$

straightforward for several reasons: (i) the different selection criteria on which the various samples are based, which may led to selection biases; (ii) the different resolution of the observations, which may result in comparison of different components because of the mismatch in the spatial scale; (iii) the different frequency coverage, as at different frequencies emission from different components is expected to dominate, and the spectral shape may change; (iv) the different sensitivity, as pre-upgrade observations (like the ones concerning work cited before) were characterized by higher rms with respect to post-upgrade observations[7] (like the ones presented here), which translates into different flux limits and therefore different detection rates. A proper comparison, although only at higher frequencies, can be carried out with the 22 GHz, 1 arcsec characterization of *Swift*/BAT hard-X-ray-selected AGN made by Smith et al. (2016, 2020), in which they report a high (∼96/100) detection rate, compatible with our estimate within the uncertainty at the same frequency.

As reported in Paper I, the detection rate of radio emission at high frequencies is larger than what has been reported in recent studies about mm emission in a handful of RQ AGN (e.g. Behar et al. 2015, 2018). Moreover, if we compare with the results obtained for low-luminosity AGN (LLAGN) only, then our detection rates are larger not only at the higher frequencies (e.g. Doi et al. 2011), but also at the lower ones (see for comparison e.g. Ho & Ulvestad 2001; Saikia et al. 2018; Chiaraluce et al. 2019).

5.2 Morphology

According to the morphological classification presented in the previous section, we find a prevalence of compact sources, either

[7]The post-upgrade VLA can reach 4 μJy beam^{-1} (1σ, in 1 h) continuum sensitivity at most bands, one order of magnitude lower than pre-upgrade VLA (e.g. van Moorsel 2014).

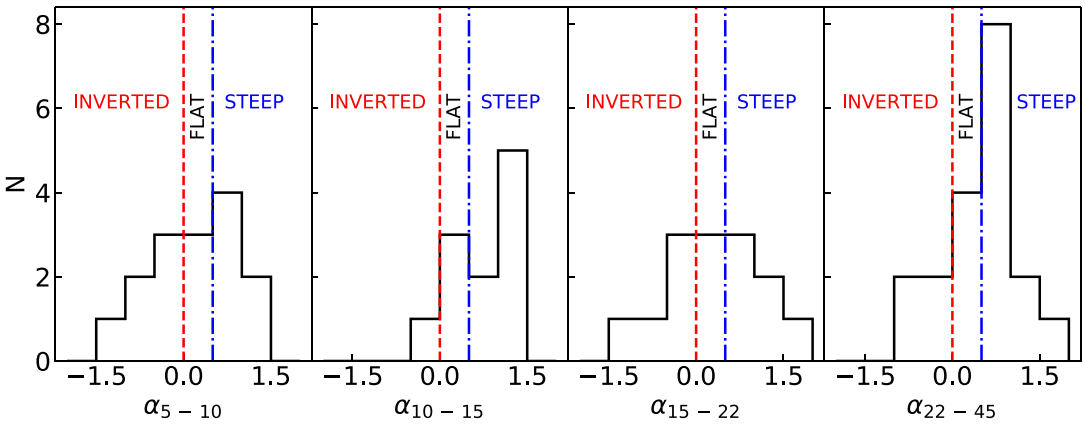

Figure 5. Histogram showing the distribution of two bands spectral indices ($S_\nu^1 \propto \nu^{-\alpha}$) for the core components of sources in this work, i.e. α_{5-10}, α_{10-15}, α_{15-22}, and α_{22-45} from left to right. The region with $\alpha < 0$ and delimited by the red dashed line represents the 'inverted' regime; the region with $0 < \alpha < 0.5$ between the red dashed and the blue dot–dashed lines represents the 'flat' regime; the region with $\alpha > 0.5$ and delimited by the blue dot–dashed line represents the 'steep' regime, according to the adopted definitions.

unresolved/slightly resolved (17/28, ∼61 per cent), with the remaining sources exhibiting jet-like features, as well as triple and more complex morphologies.

Previous surveys on Seyfert galaxies have found morphologies in similar proportions, in which however the relative fraction depends on the frequency band, as the detection fraction of extended structures are higher at low frequencies, while the fraction of compact ones increase at higher frequencies (e.g. Ulvestad et al. 1981; van der Hulst et al. 1981; Kukula et al. 1998; Nagar et al. 1999; Leipski et al. 2006; Baldi et al. 2018, 2021b). Gallimore et al. (2006) found that, for a sample of Seyfert galaxies observed at 5 GHz with compact (D) configuration of the VLA (therefore lower angular resolution ∼15–20 arcsec), the fraction of sources exhibiting kiloparsec-scale radio structures (KSRs) are significantly higher (∼45 per cent). They suggest that the lower fraction of extended sources found in a number of works (e.g. Ulvestad & Wilson 1989; Kukula et al. 1995; Schmitt et al. 2001; Thean et al. 2001) may be due to the high resolution, which resolves out the extended, low-surface brightness, steep-spectrum emission, with the KSRs being likely associated with the nuclear AGN jet activity. For our sources presented here, it is not possible to rule out that in a number of them low surface brightness emission, may be present as well.

In Smith et al. (2016, 2020), a compact component in all the detected sources is found. In more than a half (55/96) of the sample, this is the only component (either unresolved or slightly resolved), in agreement with our findings, while in 11/96 sources jet-like structures on sub-kpc to kpc scales are present. However, they find a significant number of sources (30/96) with a diffuse morphology (i.e. extended but non-linear), which they attribute to nuclear star formation.

5.3 Radio nuclear spectral energy distribution

The radio spectral slope in RQ AGN is likely the result of the combination of different emitting components dominating at different frequencies. Star formation typically produces a synchrotron steep spectrum in the 1–10 GHz regime, while a compact core is characterized by a flat or inverted spectrum (Chen et al. 2022). An AGN wind/outflow and an extended jet produce an optically thin synchrotron steep spectrum (Panessa et al. 2019).

In our sample, we find a prevalence of single power-law spectra, with the number of flat spectra equal to the number of steep spectra. If we include also single power-law sources with only two data points, then the flat spectra are nine, while the steep ones are 11.

In Fig. 6, we have plotted the mean SED obtained by calculating the mean of the slopes of the cores between two frequencies from Table 3 represented in F_ν in arbitrary units. The average trend is that of a nearly flat slope that steepens with increasing frequency, a major steepening is observed between 15 and 22 GHz. It is interesting to note that between 22 and 45 GHz the slope flattens again. This suggests that the core emission is generally optically thick below 15 GHz, in agreement with the results presented in Laor et al. (2019) for quasars with a similar range of Eddington ratios. It becomes optically thin above 15 GHz and between 22 and 45 GHz it becomes optically thick again. If we assume that the emission is produced by synchrotron, the size of the emitting region at 15 GHz is smaller than the broad-line region size (from equation 22 in Laor & Behar 2008). At higher frequencies, another emitting source should be even smaller, as higher frequency emission originates at smaller radii, and the flat spectrum can be the result of the emissivity integrated over the emitting volume. An increased radio emission is indeed expected if the observed 'mm-excess' component is extrapolated down to 45 GHz (Laor & Behar 2008; Behar et al. 2018).

5.4 Radio–X-ray correlations

It has been found that both XRBs and AGN follow tight X-ray versus radio luminosity correlations, with two different tracks, i.e. one characterized by a slope of ∼0.8 and followed by low-hard state XRBs and LLAGN (e.g. Gallo, Fender & Pooley 2003; Salvato, Greiner & Kuhlbrodt 2004; Panessa et al. 2007; Chiaraluce et al. 2019), and one characterized by a slope of ∼1.4 and followed by 'outliers' XRBs and bright RQ AGN (e.g. Coriat et al. 2011; Dong et al. 2014; Panessa et al. 2015). The scaling with the black hole mass has led to the formulation of the Fundamental Plane of black hole activity (e.g. Merloni et al. 2003; Bonchi et al. 2013; Dong et al. 2014), and to theories unifying the accretion–ejection physics of XRBs and AGN (e.g. Körding, Jester & Fender 2006). Typically, a flat slope of ∼0.8 is associated with radiatively inefficient accretion flows (e.g. Falcke et al. 2004; Coriat et al. 2011; Dong & Wu 2015), while a steep slope of ∼1.4 is associated with radiatively efficient accretion flows (e.g. Coriat et al. 2011; Gallo, Miller & Fender 2012; Dong et al. 2014; Fender & Gallo 2014; Qiao & Liu 2015).

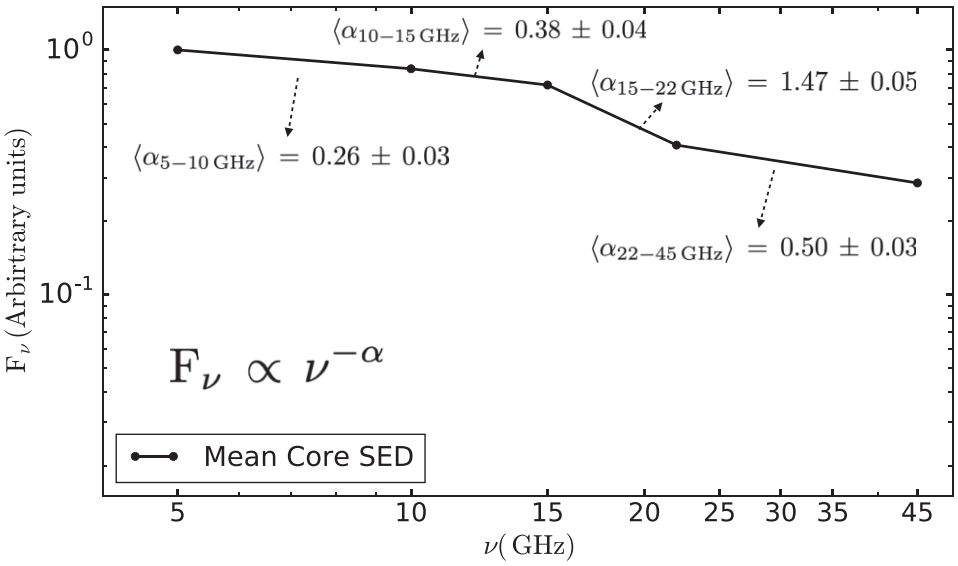

Figure 6. Mean nuclear SED in F_ν between 5 and 45 GHz obtained by calculating the mean of the two frequencies spectral slopes of the cores reported in Table 3 and plotted in arbitrary units.

In Table 5, we summarize the results of the correlations between the peak radio luminosities of the core components and the X-ray ones. In Fig. 7, we show the plots of the corresponding correlations (left-hand panel). Since in 22 and 45 GHz bands censored data in the peak radio luminosities were present, in order to estimate the slopes we used the expectation–maximization (EM) algorithm in the Astronomy Survival Analysis (ASURV Rev 1.2) software package (Isobe et al. 1990; Lavalley, Isobe & Feigelson 1992), which implements the methods presented in Isobe, Feigelson & Nelson (1986).

In order to strengthen the validity of the radio versus X-ray correlation, we have checked the significance of the corresponding flux–flux correlations. In Table 1 in Supplementary Material, we report the statistical values associated with flux–flux relations, and they are plotted in Fig. 1 in Supplementary Material. The radio versus 2–10 keV flux–flux relations are strong ($r \sim 0.6$–0.8) and significant ($P \leq 10^{-3}$), while in the case in which 20–100 keV fluxes are considered the significance is lower ($\sim 10^{-2}$).

The slopes of the luminosity–luminosity relations at all frequencies (blue dashed lines in the plots), except at 10 GHz, are compatible with the slope of 1.4 found in the case of radiatively efficient sources, with high correlations coefficients and significance at 5 and 15 GHz, while at 22 and 45 GHz, where upper limits are present, the correlations are weaker and the significance is lower (order $\sim 10^{-3}$).

In Fig. 7, the well-known powerful radio sources previously mentioned occupy a different locus. For this reason we investigated the same correlations excluding the 'offset' sources (red dot–dashed lines). The slopes obtained in this case tend to be flatter with respect to the previous case, with values in the range 0.6–1.2 and, although the correlations are strong ($r \sim 0.6$–0.8), the significance of the relations is lower, i.e. $\sim 10^{-3}$. This is expected, as the powerful radio sources occupy the high-luminosity region of the plane with the result of driving the overall relation (e.g. Hardcastle, Evans & Croston 2009).

We investigated also the existence of correlations between the peak radio luminosity and hard-X-ray (i.e. 20–100 keV) one (right-hand panel of Fig. 7), finding strong correlations ($\rho = 0.5$–0.7) with slopes in the range 1.3–2, with a high significance (order of $\sim 10^{-3}$–10^{-4}). When the 'offset' sources are excluded, in analogy with radio–X-ray correlations, the slope flatten ($\sim$0.6–1.1) and, although strong ($\rho = 0.8$–0.6), the significance is lower ($\sim 10^{-2}$).

The slopes of the radio–X-ray luminosity correlations are compatible with 1.4 found by Panessa et al. (2015) using the complete sample of 79 hard-X-ray-selected Seyferts and 1.4 GHz data ($\sim$10 per cent of RL sources are present in their sample). However, the radio observations in Panessa et al. (2015) are at 1.4 GHz and have a resolution of $\sim$45 arcsec, much larger than ours. Therefore, the flux densities and luminosities considered for the relation may be contaminated by contribution from extended, off-nuclear component, which may be not directly AGN related. Moreover, they consider all the 79 Seyferts in the sample of Malizia et al. (2009), including several powerful radio sources. Our slopes are also consistent with the findings presented in Dong et al. (2014) for a sample of bright RQ AGN with similar properties (i.e. Eddington ratios larger than 1 per cent and relatively low redshift, $z \leq 0.3$), compatible with a radiatively efficient accretion regime as postulated in AGN–XRBs unification theories. However, when powerful radio sources are excluded, the slopes become flatter. The peak of the distribution of Eddington ratios of the sources in our work is in the range between -2.25 and -1.5, while that of Dong et al. (2014), is in the range between -1 and -0.5. Our result would suggest that when intermediate accretion regimes are considered, the slope of the relation flattens, with values that are intermediate between the 0.8 slope for the very low accretion regimes and the slope of 1.4 for higher accretion regimes.

With these observations we can test if the sources follow the empirical $L_R/L_X \sim 10^{-5}$ relation valid for coronally active stars. The finding that also bright RQ AGN follow the relation has been interpreted in light of models in which both radio and X-ray would come from a hot corona (e.g. Laor & Behar 2008). In the left-hand panel of Fig. 7, the solid black line represents the above relation. We find that at 5 and 10 GHz the sources, except for the offset ones, roughly follow the relation, but at higher frequencies (15, 22, and 45 GHz) their peak radio luminosities tend to be systematically above the relation. In order to quantify this effect, we calculated

Table 5. Results of the correlation between peak radio luminosities of the core components and the 2–10 keV luminosities, for all the sample and excluding the offset sources. Associated flux–flux correlations are also reported. Column (1): the relation; column (2): sample considered; column (3): the slope of the relation (log–log); column (4): the intercept; column (5): Spearman's rank correlation coefficient; column (6): probability of the null hypothesis that null hypothesis is that two sets of data are uncorrelated; column (7): Kendall's tau; column (8): probability of the null hypothesis.

Relation	Sample	m (slope)	q (intercept)	ρ (Spearman)	P-value (Spearman)	τ (Kendall's)	P-value (Kendall's)
(1)	(2)	(3)	(4)	(5)	(6)	(7)	(8)
$\log L^{\rm peak}_{5\,\rm GHz}$–$\log L_{2-10\,\rm keV}$	All	1.63 ± 0.23	-32 ± 10	0.8	9×10^{-6}	0.64	5×10^{-5}
	RQ	1.05 ± 0.25	-7 ± 11	0.7	1×10^{-3}	0.5	2×10^{-3}
$\log F^{\rm peak}_{5\,\rm GHz}$–$\log F_{2-10\,\rm keV}$	All	1.33 ± 0.42	-4 ± 5	0.6	7×10^{-3}	0.4	6×10^{-3}
	RQ	1.33 ± 0.40	-4 ± 5	0.6	7×10^{-3}	0.4	7×10^{-3}
$\log L^{\rm peak}_{10\,\rm GHz}$–$\log L_{2-10\,\rm keV}$	All	1.77 ± 0.24	-38 ± 10	0.7	2×10^{-4}	0.6	3×10^{-4}
	RQ	1.16 ± 0.25	-12 ± 11	0.6	1×10^{-2}	0.4	1×10^{-2}
$\log F^{\rm peak}_{10\,\rm GHz}$–$\log F_{2-10\,\rm keV}$	All	1.36 ± 0.42	-3 ± 5	0.64	2×10^{-3}	0.5	3×10^{-3}
	RQ	1.37 ± 0.40	-3 ± 5	0.6	2×10^{-3}	0.5	3×10^{-3}
$\log L^{\rm peak}_{15\,\rm GHz}$–$\log L_{2-10\,\rm keV}$	All	1.55 ± 0.30	-29 ± 11	0.8	2×10^{-5}	0.6	1×10^{-4}
	RQ	1.07 ± 0.20	-8 ± 9	0.76	3×10^{-4}	0.6	1×10^{-3}
$\log F^{\rm peak}_{15\,\rm GHz}$–$\log F_{2-10\,\rm keV}$	All	1.16 ± 0.40	-5 ± 5	0.6	7×10^{-3}	0.4	9×10^{-3}
	RQ	1.15 ± 0.44	-5.4 ± 4.9	0.6	7×10^{-3}	0.43	9×10^{-3}
$\log L^{\rm peak}_{22\,\rm GHz}$–$\log L_{2-10\,\rm keV}$[a]	All	1.4 ± 0.4	-23 ± 17	0.64	1×10^{-3}	$z \sim 3.5$	4×10^{-4}
	RQ	0.81 ± 0.21	3.6 ± 9.0	0.7	1.4×10^{-3}	$z \sim 3.2$	1.5×10^{-3}
$\log F^{\rm peak}_{22\,\rm GHz}$–$\log F_{2-10\,\rm keV}$[a]	All	1.4 ± 0.5	-3 ± 5	0.6	2×10^{-3}	$z \sim 3.2$	1×10^{-3}
	RQ	1.05 ± 0.30	-6.8 ± 3.0	0.6	5×10^{-3}	$z \sim 3.17$	1.5×10^{-3}
$\log L^{\rm peak}_{45\,\rm GHz}$–$\log L_{2-10\,\rm keV}$[a]	All	1.33 ± 0.40	-18 ± 17	0.6	3×10^{-3}	$z \sim 3.4$	7×10^{-4}
	RQ	0.71 ± 0.2	8 ± 8	0.6	6×10^{-3}	$z \sim 3.04$	2×10^{-3}
$\log F^{\rm peak}_{45\,\rm GHz}$–$\log F_{2-10\,\rm keV}$[a]	All	1.4 ± 0.5	-3 ± 6	0.6	2×10^{-3}	$z \sim 3.3$	1×10^{-3}
	RQ	1.0 ± 0.3	-7.4 ± 3.0	0.6	4×10^{-3}	$z \sim 3.23$	1×10^{-3}

[a]For K and Q bands, since upper limits in the dependent variables were present, the reported values are from the EM regression algorithm, the Spearman's rho and the generalized Kendall's tau calculated in the ASURV package.

mean values of the quantity $\log L_{\rm R}/L_{\rm X}$ for the non-offset sources,[8] considering different radio luminosities, with the KMESTM routine in the ASURV package.[9] The mean values are -4.9 ± 0.1 at 5 GHz, -4.8 ± 0.1 at 10 GHz, -4.6 ± 0.1 at 15 GHz, -4.8 ± 0.1 at 22 GHz, and -4.5 ± 0.1 at 45 GHz,[10] with an increase of $\log L_{\rm R}/L_{\rm X}$ ratio with frequency. We note that the $\log L_{\rm R}/L_{\rm X}$ relation has been found considering the 5 GHz luminosity (e.g. Laor & Behar 2008), while Behar et al. (2018) found that when high frequencies (i.e. at $\sim$100 GHz) are considered, the relation rather follow a $\sim 10^{-4}$ trend. Indeed, we find that as the frequency increases, the sources tend to cluster in this intermediate regime.

There is still no definite explanation for the observed functional form of relation and care should be taken when deriving physical conclusions based on them. Indeed, several works reported that different slopes are found when considering different classes of objects, i.e. only RL sources (Wang, Wu & Kong 2006), gigahertz peaked and compact steep spectrum sources (GPS and CSS; e.g. Fan & Bai 2016), Narrow-Line Seyfert 1 (NLS1; e.g. Yao et al. 2018), and blazars (Zhang, Zhang & Zhang 2018). Magnetically dominated coronae may explain the observed relations in RQ AGN (e.g. Laor & Behar 2008, and references therein). Alternatively, an interpretation in terms of a coupling of inflow and outflow as in XRBs may apply (e.g. Carotenuto et al. 2021, and references therein).

[8]The offset sources, as expected, are characterized by $\log L_{\rm R}/L_{\rm X} \geq -3$.
[9]The routine KMESTM gives the Kaplan–Meier estimator for the distribution function of a randomly censored sample.
[10]In the case in which the smallest value is an upper limit the mean may suffer from statistical biases, for details see the ASURV documentation.

6 CLUES ON THE ORIGIN OF NUCLEAR RADIO EMISSION

Four sources in our sample are well-known powerful radio emitters QSO B0241+62, B3 0309+411B, NGC 1275, and 4C +74.26. Their radio properties are consistent with the jet activity already reported by previous studies (e.g. Hutchings et al. 1982; de Bruyn 1989; Pedlar et al. 1990; Ho & Ulvestad 2001; Healey et al. 2007; Lister et al. 2019; Bruni et al. 2020).

The remaining sources (26/30) can be classified as RQ considering their radio properties. Two of them are undetected (IGR J16426+6536 and IGR J18027−1455) and one of them (2E 1853.7+1534) has been detected at 22 GHz (only 22 and 45 GHz observation were available) resulting in a diffuse component that maybe consistent with jet/outflow or starburst emission.

Steep spectra are found in 11/30 sources. Five of them, namely NGC 1068, MCG +08-11-11, Mrk 3, Mrk 6, and NGC 4388, exhibit resolved, jet-like structure, sometimes coupled to more complex features. For these sources, the origin of observed radio emission is compatible with optically thin synchrotron emission from a subrelativistic jet. This in agreement with previous studies reporting aligned structures on mas scales, high brightness temperature ($\gg 10^8$ K), and flat spectrum for the mas cores (e.g. Kukula et al. 1996, 1999; Lal, Shastri & Gabuzda 2004). However, in NGC 1068 and NGC 4388, while a jet is observed at kpc and sub-kpc scales, mas scales observations revealed low brightness temperature cores ($\sim 10^5$ K), compatible with thermal free–free emission from the inner torus (e.g. Gallimore et al. 1996; Kukula et al. 1999; Mundell et al. 2000; Giroletti & Panessa 2009). Six sources, namely NGC 4151, IGR J00333+6122, LEDA 168563, NGC 5506, IGR J1638−2057, and IGR J20186+4043, exhibit a compact morphology and a steep

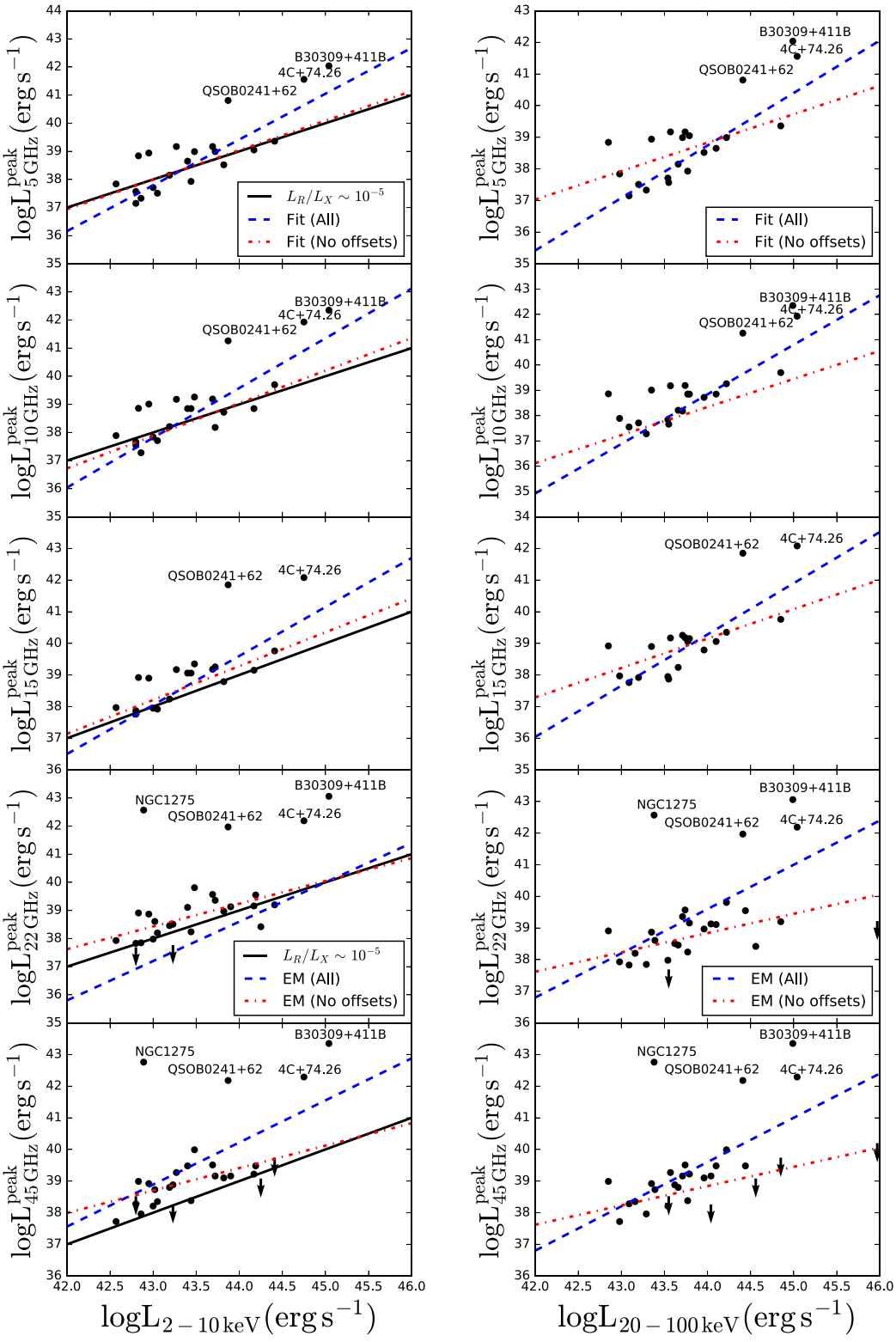

Figure 7. Plots of the correlations between peak radio luminosities of the core components and X-ray (2–10 keV, left-hand panel) and hard-X-ray (20–100 keV, right-hand panel) ones. From top to bottom: 5, 10, 15, 22, and 45 GHz bands. The solid black line is the $L_{\rm R}/L_{\rm X} \sim 10^{-5}$ relation; the dashed blue line represents a regression considering all the data, the red dot–dashed line represents a regression discarding the offset sources (i.e. QSO B0241+62, B3 0309+411B, NGC 1275, and 4C +74.26, see the text). In the case of 22 and 45 GHz bands, since upper limits were present, the regression lines are calculated from an EM algorithm.

spectrum. In this case, the observed radio emission may be due to optically thin emission from a subrelativistic jet that is unresolved by our observations, as already observed in NGC 4151 and NGC 5506 (e.g. Pedlar et al. 1993; Mundell et al. 2003; Middelberg et al. 2004; Ulvestad et al. 2005). Radio emission from star formation may instead occur at larger (a few kpc) scales (e.g. Padovani et al. 2011; Condon et al. 2013). For the remaining sources optically thin synchrotron emission from disc winds cannot be ruled out and higher resolution observations are needed.

Three sources, namely IGR J23524+5842, NGC 4593, and IGR J13091+1137, exhibit peaked spectra in the GHz range. The source IGR J23524+5842 exhibits a core coupled to a one-sided lobe, and its radio emission likely comes from a jet; for the other two this hypothesis cannot be confirmed, as they are compact and the SED exhibits an additional component at high frequencies.

Two more sources, namely NGC 5252 and NGC 1142, exhibit cores with flat spectra up to a break (at ∼10 and ∼15 GHz, respectively). This emission is likely due to a jet, the subsequent spectral decline is probably marking the transition to the optically thin regime. In the former, the non-thermal origin of radio emission has been confirmed by very long baseline interferometry (VLBI) studies (e.g. Mundell et al. 2000), while in the latter this scenario cannot be confirmed. The extranuclear radio emission of NGC 1142 is of star formation origin and it is discussed in a dedicated section in Appendix A.

Finally, seven sources, namely NGC 788, 4U 0517+17, Mrk 50, LEDA 170194, IGR J17513−2011, IGR J18259−0706, and IGR J23308+7120, exhibit compact flat-spectrum cores. In addition to the flat core, LEDA 170194 shows a steep-spectrum two-sided jet extending over ∼2 kpc.

The observed radio sources above exhibit flat spectra up to 45 GHz (with the exception of IGR J23308+7120, which is flat up to 15 GHz and undetected at 22 and 45 GHz). This may be due to optically thick synchrotron emission from a compact jet. However, flat radio spectra extending up to high frequencies, may also be due to synchrotron radio emission from a magnetically heated corona (e.g. Laor & Behar 2008). In the so-called coronal models, the corona is a radially stratified plasma, both in the magnetic field and number density of relativistic electrons, in either a spherical or disc geometry. Each plasma shell emits as optically thick synchrotron radiation, but variations in the opacity from one shell to another produce different turnover frequencies, such that external shells dominate low frequencies, while inner ones dominate the high frequency range. The result is an overall flat radio spectrum (e.g. Raginski & Laor 2016). One difference between the compact jet and coronal emission scenario is that in the former a break in the spectral slope (due to the optically thick/optically thin transition) is expected at relatively low frequencies (a few tens of GHz), while the compactness of the corona can result in flat spectra up to ∼300 GHz (e.g. Laor & Behar 2008; Raginski & Laor 2016). This suggests that, with the resolution and frequency coverage of our observations, the external layers of the corona are eventually sampled.

In order to put more stringent constraints to the origin of radio emission in these sources VLBI observations will be fundamental. Indeed, it will be possible to determine the mas size of the sources, as a size smaller than ∼pc rules out star formation or an AGN wind interacting with the interstellar medium. Moreover, it will also exclude free–free emission, as a brightness temperature much larger than $\sim 10^6$ K is compatible only with non-thermal emission (e.g. Condon & Ransom 2016). Finally, variability studies can constrain the size of the emitting regions and therefore discriminate between star formation and non-thermal emission, like the base of a jet or a corona, expected to vary on relatively small timescales (e.g. Barvainis et al. 2005; Baldi et al. 2015; Panessa et al. 2022).

7 CONCLUSIONS

In this paper, we presented wide-band (5–45 GHz), high-sensitivity (a few μJy beam^{-1}), sub-arcsec (1–0.4 arcsec) JVLA observations for a sample of 30 nearby ($0.003 \leq z \leq 0.3$) and moderately accreting ($-2.5 \leq \log L/L_{\rm Edd} \leq -0.5$) hard-X-ray-selected AGN. The observations allow to characterize the sub-kpc scale radio properties of the sample and build wide-band SEDs, with the final aim of investigating the origin of radio emission. Below we summarize our main findings.

(i) We find a high detection fraction of radio emission at all frequencies that decreases with frequency (21/21, 21/21, 19/19, 26/29, and 24/29, i.e. 96, 96, 95, 87, and 81 per cent at 5, 10, 15, 22, and 45 GHz, respectively). These values occupy the high tail of the distribution of the detection rates reported in literature for RQ AGN, typically around 70–90 per cent.

(ii) The radio luminosities of the detected sources are in the range $37 \leq \log L_{\rm R}$ (erg s^{-1}) ≤ 40. Four sources are known powerful radio emitters and indeed show larger luminosities ≥41 (in log units).

(iii) Two sources (observed only at 22 and 45 GHz) have not been detected. The upper limits on their flux densities are ∼0.15 and 0.1 mJy beam^{-1}. One of them, IGR J16426+6536, has been observed twice, ∼17 months apart, in both cases it is undetected. The upper limits on radio luminosities imply values of the X-ray radio loudness $R_{\rm X} < -4.5$, at the very low power tail of radio-loudness distribution, possibly hinting to a 'radio-silent' nature.

(iv) The morphology of the sources varies with the selected frequency, where extended emission dominates the lower frequencies. Overall, the majority of them are compact, characterized by a core component (17/30). The remaining sources exhibit either one-sided (7/30) or two-sided (1/30) jets. Three sources exhibit a complex morphology.

(v) The SED of the sources can be classified into three categories: single power-law spectra (14/30), convex spectra (3/30), and BPL spectra (4/30). For 6/30 sources only two SED data points (at 22 and 45 GHz) are available, while for one source only one data point is available. We derive a mean radio SED of the cores.

(vi) We find a significant radio–X-ray correlation at all frequencies. When the four powerful radio emitters are excluded, the slopes of the correlation range $m = 0.7$–1.2. This range is intermediate between the slope of 1.4 found for high-luminosity AGN and the slope of 0.8 found for LLAGN, in agreement with the intermediate accretion rates and luminosities covered by the sample considered here.

(vii) Our sources roughly follow the empirical Gudel–Benz relation, with a transition from the 10^{-5} to the 10^{-4} relation at higher frequencies (i.e. 15, 22, and 45 GHz), suggesting a possible contribution to both radio and X-ray from a hot corona. The four powerful radio emitters significantly depart from the relation, as expected.

The combination of morphology, SED shape, and (when available) VLBI information from the literature allows to formulate possible scenarios for the radiative mechanisms responsible for the radio emission: (i) ∼13 per cent of the sample is RL; (ii) ∼37 per cent of the sample has steep spectra compatible with optically thin synchrotron from a jet, which is unresolved in compact cores. In ∼13 per cent of them, optically thin synchrotron from disc winds cannot be ruled out; (iii) flat spectrum sources are generally compact (except for LEDA 170194 that exhibits a two-sided jet), indicating a possible optically thick synchrotron emission from a compact jet and/or a hot corona (∼30 per cent); (iv) in ∼30 per cent of the sample, peaked core

spectra are found (in one case showing a one-sided jet morphology) again suggesting a possible jet scenario.

This work is part of a large project aiming at investigating the origin of radio emission through high-resolution, high-sensitivity, multi-epoch, wide-band radio observations. Our volume-limited, well-characterized hard-X-ray sample is perfectly suited to push over this effort by exploiting the unprecedented capabilities of the Square Kilometre Array (SKA) pathfinders and precursors.

ACKNOWLEDGEMENTS

We acknowledge the anonymous referee for valuable suggestions and comments that have improved the quality of our paper. The authors would like to thank the National Radio Astronomy Observatory (NRAO) help desk staff for the help in the data reduction. The NRAO is a facility of the National Science Foundation operated under cooperative agreement by Associated Universities, Inc. EC acknowledges the National Institute of Astrophysics (INAF) and the University of Rome Tor Vergata for the PhD scholarship in the XXXIII PhD cycle for the period 2017 December–2020 December. GB and FP acknowledge financial support under the *INTEGRAL* ASI-INAF agreement 2019-35-HH.0. Part of the data reduction has been performed by EC at the DiFA – University of Bologna and the Istituto di Radioastronomia in the period 2010 January–March, a visit funded by the Bando Fondi Ricerca 2019 of the INAF-IAPS. FP acknowledges support from a grant PRIN-INAF SKA-CTA 2016. AL was supported by the Israel Science Foundation (grant no. 1008/18). EB is supported by a Center of Excellence of the Israel Science Foundation (grant no. 2752/19). IM thanks STFC for support under grant ST/R000638/1. FT acknowledges support by the Programma per Giovani Ricercatori – anno 2014 Rita Levi Montalcini. This research made use of APLPY, an open-source plotting package for PYTHON (Robitaille & Bressert 2012).

DATA AVAILABILITY

The data underlying this paper were accessed from NRAO (https://science.nrao.edu/). The derived data generated in this research will be shared on reasonable request to the corresponding author.

REFERENCES

Antonucci R., Barvainis R., 1988, ApJ, 332, L13
Appleton P. N., Charmandaris V., Gao Y., Jarrett T., Bransford M. A., 2003, ApJ, 586, 112
Baldi R. D., Behar E., Laor A., Horesh A., 2015, MNRAS, 454, 4277
Baldi R. D. et al., 2018, MNRAS, 476, 3478
Baldi R. D. et al., 2021a, MNRAS, 500, 4749
Baldi R. D. et al., 2021b, MNRAS, 508, 2019
Baldi R. D., Laor A., Behar E., Horesh A., Panessa F., McHardy I., Kimball A., 2022, MNRAS, 510, 1043
Barvainis R., Lonsdale C., Antonucci R., 1996, AJ, 111, 1431
Barvainis R., Lehár J., Birkinshaw M., Falcke H., Blundell K. M., 2005, ApJ, 618, 108
Bassani L., Venturi T., Molina M., Malizia A., Dallacasa D., Panessa F., Bazzano A., Ubertini P., 2016, MNRAS, 461, 3165
Behar E., Baldi R. D., Laor A., Horesh A., Stevens J., Tzioumis T., 2015, MNRAS, 451, 517
Behar E., Vogel S., Baldi R. D., Smith K. L., Mushotzky R. F., 2018, MNRAS, 478, 399
Bonchi A., La Franca F., Melini G., Bongiorno A., Fiore F., 2013, MNRAS, 429, 1970
Briggs D. S., 1995, BAAS, 27, 1444
Bruni G. et al., 2020, MNRAS, 494, 902
Calzetti D. et al., 2007, ApJ, 666, 870
Carotenuto F. et al., 2021, MNRAS, 505, L58
Chen S. et al., 2022, MNRAS, 512, 471
Chiaraluce E., Bruni G., Panessa F., Giroletti M., Orienti M., Rampadarath H., Vagnetti F., Tombesi F., 2019, MNRAS, 485, 3185
Chiaraluce E., Panessa F., Bruni G., Baldi R. D., Behar E., Vagnetti F., Tombesi F., McHardy I., 2020, MNRAS, 495, 3943 (Paper I)
Condon J. J., 1992, ARA&A, 30, 575
Condon J. J., Ransom S. M., 2016, Essential Radio Astronomy. Princeton Univ. Press, Princeton, NJ
Condon J. J., Helou G., Sanders D. B., Soifer B. T., 1990, ApJS, 73, 359
Condon J. J., Kellermann K. I., Kimball A. E., Ivezić Ž., Perley R. A., 2013, ApJ, 768, 37
Coriat M. et al., 2011, MNRAS, 414, 677
de Bruyn A. G., 1989, A&A, 226, L13
Doi A., Nakanishi K., Nagai H., Kohno K., Kameno S., 2011, AJ, 142, 167
Dong A.-J., Wu Q., 2015, MNRAS, 453, 3447
Dong A.-J., Wu Q., Cao X.-F., 2014, ApJ, 787, L20
Falcke H., Malkan M. A., Biermann P. L., 1995, A&A, 298, 375
Falcke H., Körding E., Markoff S., 2004, A&A, 414, 895
Fan X.-L., Bai J.-M., 2016, ApJ, 818, 185
Fender R., Gallo E., 2014, Space Sci. Rev., 183, 323
Ferrarese L., Merritt D., 2000, ApJ, 539, L9
Ferreira J., Deguiran R., 2013, High Energy Density Phys., 9, 67
Gallimore J. F., Baum S. A., O'Dea C. P., Pedlar A., 1996, ApJ, 458, 136
Gallimore J. F., Axon D. J., O'Dea C. P., Baum S. A., Pedlar A., 2006, AJ, 132, 546
Gallo E., Fender R. P., Pooley G. G., 2003, MNRAS, 344, 60
Gallo E., Miller B. P., Fender R., 2012, MNRAS, 423, 590
Gao Y., Solomon P. M., Downes D., Radford S. J. E., 1997, ApJ, 481, L35
Giroletti M., Panessa F., 2009, ApJ, 706, L260
Gültekin K. et al., 2009, ApJ, 698, 198
Hardcastle M. J., Evans D. A., Croston J. H., 2009, MNRAS, 396, 1929
Healey S. E., Romani R. W., Taylor G. B., Sadler E. M., Ricci R., Murphy T., Ulvestad J. S., Winn J. N., 2007, ApJS, 171, 61
Hippelein H. H., 1989, A&A, 216, 11
Ho L. C., Ulvestad J. S., 2001, ApJS, 133, 77
Högbom J. A., 1974, A&AS, 15, 417
Hutchings J. B., Campbell B., Gower A. C., Crampton D., Morris S. C., 1982, ApJ, 262, 48
Isobe T., Feigelson E. D., Nelson P. I., 1986, ApJ, 306, 490
Isobe T., Feigelson E. D., Akritas M. G., Babu G. J., 1990, ApJ, 364, 104
Jiang Y.-F., Ciotti L., Ostriker J. P., Spitkovsky A., 2010, ApJ, 711, 125
Joy M., Ghigo F. D., 1988, ApJ, 332, 179
Kellermann K. I., Sramek R., Schmidt M., Shaffer D. B., Green R., 1989, AJ, 98, 1195
Körding E. G., Jester S., Fender R., 2006, MNRAS, 372, 1366
Körding E., Rupen M., Knigge C., Fender R., Dhawan V., Templeton M., Muxlow T., 2008, Science, 320, 1318
Kormendy J., Richstone D., 1995, ARA&A, 33, 581
Kukula M. J., Pedlar A., Baum S. A., O'Dea C. P., 1995, MNRAS, 276, 1262
Kukula M. J., Holloway A. J., Pedlar A., Meaburn J., Lopez J. A., Axon D. J., Schilizzi R. T., Baum S. A., 1996, MNRAS, 280, 1283
Kukula M. J., Dunlop J. S., Hughes D. H., Rawlings S., 1998, MNRAS, 297, 366
Kukula M. J., Ghosh T., Pedlar A., Schilizzi R. T., 1999, ApJ, 518, 117
Lal D. V., Shastri P., Gabuzda D. C., 2004, A&A, 425, 99
Lamb S. A., Hearn N. C., Gao Y., 1998, ApJ, 499, L153
Laor A., Behar E., 2008, MNRAS, 390, 847
Laor A., Baldi R. D., Behar E., 2019, MNRAS, 482, 5513
Laplace P.-S., 1812, Théorie Analytique Des Probabilités. Courcier, Paris, available at https://www.bibsonomy.org/bibtex/28c4c8f12f315e3886329d64df7597fd8/vatchoum
Lavalley M., Isobe T., Feigelson E., 1992, in Worrall D. M., Biemesderfer C., Barnes J., eds, ASP Conf. Ser. Vol. 25, Astronomical Data Analysis Software and Systems I. Astron. Soc. Pac., San Francisco, p. 245
Leipski C., Falcke H., Bennert N., Hüttemeister S., 2006, A&A, 455, 161
Lister M. L. et al., 2019, ApJ, 874, 43

McMullin J. P., Waters B., Schiebel D., Young W., Golap K., 2007, in Shaw R. A., Hill F., Bell D. J., eds, ASP Conf. Ser. Vol. 376, Astronomical Data Analysis Software and Systems XVI. Astron. Soc. Pac., San Francisco, p. 127
Magorrian J. et al., 1998, AJ, 115, 2285
Malizia A., Stephen J. B., Bassani L., Bird A. J., Panessa F., Ubertini P., 2009, MNRAS, 399, 944
Merloni A., Heinz S., di Matteo T., 2003, MNRAS, 345, 1057
Mezcua M., Roberts T. P., Sutton A. D., Lobanov A. P., 2013, MNRAS, 436, 3128
Middelberg E. et al., 2004, A&A, 417, 925
Morganti R., 2017, Frontiers Astron. Space Sci., 4, 42
Mundell C. G., Wilson A. S., Ulvestad J. S., Roy A. L., 2000, ApJ, 529, 816
Mundell C. G., Wrobel J. M., Pedlar A., Gallimore J. F., 2003, ApJ, 583, 192
Nagar N. M., Wilson A. S., Mulchaey J. S., Gallimore J. F., 1999, ApJS, 120, 209
Nagar N. M., Falcke H., Wilson A. S., Ulvestad J. S., 2002, A&A, 392, 53
Nyland K. et al., 2020, ApJ, 905, 74
Padovani P., 2016, A&AR, 24, 13
Padovani P., Miller N., Kellermann K. I., Mainieri V., Rosati P., Tozzi P., 2011, ApJ, 740, 20
Panessa F., Giroletti M., 2013, MNRAS, 432, 1138
Panessa F., Bassani L., Cappi M., Dadina M., Barcons X., Carrera F. J., Ho L. C., Iwasawa K., 2006, A&A, 455, 173
Panessa F., Barcons X., Bassani L., Cappi M., Carrera F. J., Ho L. C., Pellegrini S., 2007, A&A, 467, 519
Panessa F. et al., 2015, MNRAS, 447, 1289
Panessa F., Baldi R. D., Laor A., Padovani P., Behar E., McHardy I., 2019, Nat. Astron., 3, 387
Panessa F. et al., 2022, MNRAS, 510, 718
Pedlar A., Ghataure H. S., Davies R. D., Harrison B. A., Perley R., Crane P. C., Unger S. W., 1990, MNRAS, 246, 477
Pedlar A., Kukula M. J., Longley D. P. T., Muxlow T. W. B., Axon D. J., Baum S., O'Dea C., Unger S. W., 1993, MNRAS, 263, 471
Perley R. A., Butler B. J., 2017, ApJS, 230, 7
Planck Collaboration VI, 2020, A&A, 641, A6
Price D. J., Pringle J. E., King A. R., 2003, MNRAS, 339, 1223
Qiao E., Liu B. F., 2015, MNRAS, 448, 1099
Raginski I., Laor A., 2016, MNRAS, 459, 2082
Robitaille T., Bressert E., 2012, Astrophysics Source Code Library, record ascl:1208.017
Roy A. L., Colbert E. J. M., Wilson A. S., Ulvestad J. S., 1998, ApJ, 504, 147
Saikia P., Körding E., Coppejans D. L., Falcke H., Williams D., Baldi R. D., Mchardy I., Beswick R., 2018, A&A, 616, A152
Salvato M., Greiner J., Kuhlbrodt B., 2004, ApJ, 600, L31
Sánchez S. F. et al., 2012, A&A, 538, A8
Sauro J., Lewis J. R., 2005, in Proc. Human Factors and Ergonomics Society 49th Annual Meeting. Human Factors and Ergonomics Society, Santa Monica, CA, p. 2100
Scheuer P. A. G., Williams P. J. S., 1968, ARA&A, 6, 321
Schmitt H. R., Antonucci R. R. J., Ulvestad J. S., Kinney A. L., Clarke C. J., Pringle J. E., 2001, ApJ, 555, 663
Sebastian B., Kharb P., O'Dea C. P., Gallimore J. F., Baum S. A., 2020, MNRAS, 499, 334
Silpa S., Kharb P., Ho L. C., Ishwara-Chandra C. H., Jarvis M. E., Harrison C., 2020, MNRAS, 499, 5826
Smith K. L., Mushotzky R. F., Vogel S., Shimizu T. T., Miller N., 2016, ApJ, 832, 163
Smith K. L. et al., 2020, MNRAS, 492, 4216
Terashima Y., Wilson A. S., 2003, ApJ, 583, 145
Thean A., Pedlar A., Kukula M. J., Baum S. A., O'Dea C. P., 2000, MNRAS, 314, 573
Thean A. H. C., Gillibrand T. I., Pedlar A., Kukula M. J., 2001, MNRAS, 327, 369
Ulvestad J. S., Wilson A. S., 1986, MNRAS, 218, 711
Ulvestad J. S., Wilson A. S., 1989, ApJ, 343, 659
Ulvestad J. S., Wilson A. S., Sramek R. A., 1981, ApJ, 247, 419
Ulvestad J. S., Wong D. S., Taylor G. B., Gallimore J. F., Mundell C. G., 2005, AJ, 130, 936
van der Hulst J. M., Crane P. C., Keel W. C., 1981, AJ, 86, 1175
van Moorsel G., 2014, in XXXIth URSI General Assembly and Scientific Symposium (URSI GASS). IEEE, Manhattan, NY, p. 1
Wang R., Wu X.-B., Kong M.-Z., 2006, ApJ, 645, 890
Wilson A. S., Colbert E. J. M., 1995, ApJ, 438, 62
Yao S., Qiao E., Wu X.-B., You B., 2018, MNRAS, 477, 1356
Zakamska N. L., Greene J. E., 2014, MNRAS, 442, 784
Zakamska N. L. et al., 2016, MNRAS, 455, 4191
Zhang X., Zhang H., Zhang X., 2018, Ap&SS, 363, 259
Zirbel E. L., Baum S. A., 1995, ApJ, 448, 521
Zubovas K., 2019, MNRAS, 483, 1957

SUPPORTING INFORMATION

Supplementary data are available at *MNRAS* online.

HXAGN_MNRAS_2022_Supplementary.pdf

Please note: Oxford University Press is not responsible for the content or functionality of any supporting materials supplied by the authors. Any queries (other than missing material) should be directed to the corresponding author for the article.

APPENDIX A: NGC 1142

NGC 1142 is a massive spiral galaxy and is part of an interacting system Arp 118, in which the companion is the massive elliptical galaxy NGC 1143, ∼40 arcsec far away in the north-west (NW) direction (∼24 kpc). It is most probably the result of a collisional encounter (e.g. Joy & Ghigo 1988).

Its radio map exhibits a complex morphology, with a central component, named B, where the core is believed to reside, plus additional extranuclear components on scales of ∼10 kpc (total extension). At 5, 10, and 15 GHz, a southern ridge of radio emission extending on approximately the same spatial scale is visible. At 22 GHz six components are detected plus a southern ridge, namely East, A1, A2, C, B, and D. In the 45 GHz naturally weighted map only three components are detected, namely A1, A2, and B. This is due to a combined effect of the steep spectrum of the off-nuclear components and the lower sensitivity at 45 GHz with respect to 22 GHz. At 5 GHz (archival post-upgrade JVLA observations) the East component is blended with A1, while the C component is not detected. At 10 and 15 GHz the significance of the detection of the off-nuclear components is lower. This is due to a combined effect of the steep spectrum and the higher rms in these bands with respect to 5 and 22 GHz maps (archival VLA observations were of lower sensitivity before the upgrade). The observed morphology is compatible with previous radio studies at comparable resolution (e.g. Joy & Ghigo 1988; Condon et al. 1990; Thean et al. 2000), although an additional component, C, is detected with a high significance at 22 GHz.

The present observations at matched resolution, although with slightly different sensitivities, allow to build for the first time the SED for all the detected components. The core (component B) exhibit a spectrum that is flat/inverted up to a break occurring at ∼15 GHz, with a steep decline after it (see Table 4). This likely originates from the base of a jet, However, due to the missing information at the mas scale, it is not possible to rule out a possible thermal origin.

The extranuclear components are characterized by steep spectra in cm/sub-cm range, with spectral indices in the range 0.7–1.3 (see Table 4 and bottom right-hand panel of Fig. 4). These values, together with the observed morphology, are compatible with radio emission

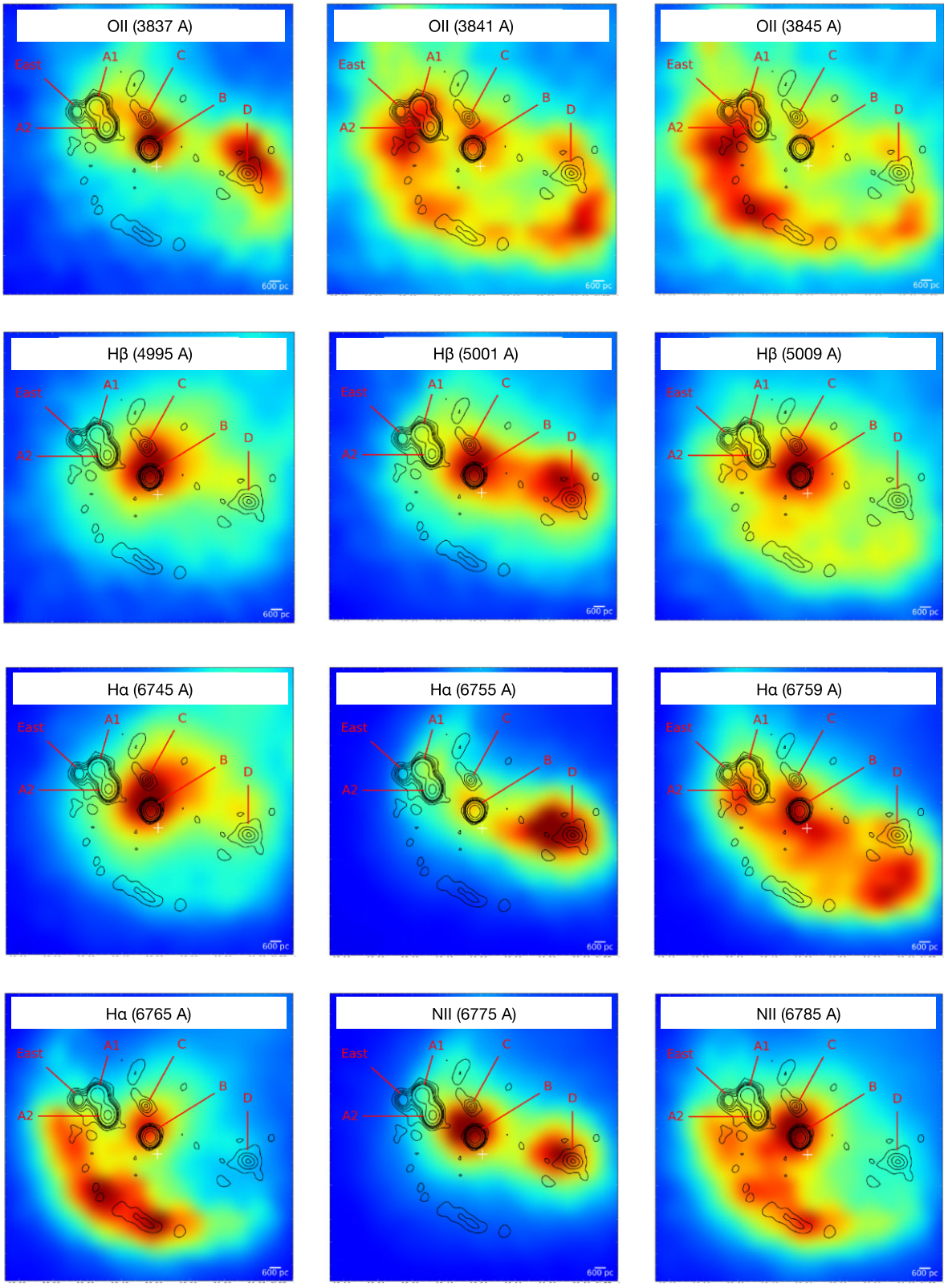

Figure A1. Maps for NGC 1142 in which we overplot our proprietary K-band contours to CALIFA emission lines maps at different wavelengths, comprising O II, Hβ, Hα, and N II. In each map, the wavelength corresponding to the optical emission line image is indicated (in Å).

from star formation (e.g. Condon 1992; Panessa et al. 2019). This source is part of the Calar Alto Legacy Integral Field Area (CALIFA) survey (Sánchez et al. 2012) that covers the range of 3700–7000 Å with a 3.7 arcsec resolution.

In Fig. A1, we show overplots of 22 GHz contours with optical emission lines images corresponding to different lines, i.e. N II, O II, Hα, and Hβ (the corresponding wavelengths of each optical map are indicated on top). These lines may trace recent star formation (e.g. Calzetti et al. 2007). From Fig. A1 it is possible to make the following considerations: (i) the component B, the nucleus, is always optically bright, as expected; (ii) the component D is bright in all emission lines; (iii) the southern ridge is bright in N II, O II, and Hα, it is weak in Hβ; (iv) the triple group East/A1/A2 is bright in O II, it is weak in Hα, Hβ, and N II.

The above considerations are suggesting that the radio emission from the extranuclear steep spectrum components, coinciding with spikes in optical emission lines maps, is indeed synchrotron radiation from regions of intense star formation, as first proposed by Joy & Ghigo (1988). Previous works support this interpretation and have found that the component D indeed coincides with a giant H II region (e.g. Hippelein 1989); the southern ridge is part of the ring of the disc galaxy that is stripped in an elliptical geometry because of encounter with the companion galaxy, which has produced an enhancement in the molecular gas density, as traced by CO(1–0) observations (e.g. Gao et al. 1997). In this scenario, the coincidence of star-forming regions traced by optical and radio observations with regions of increased gas density is supported by dynamical models (e.g. Lamb, Hearn & Gao 1998). While the interpretation of the origin of steep-spectrum radio emission of the extranuclear components D and southern ridge fits with the above picture, that of triple East/A1/A2 is not straightforward, as it appears weak in emission lines (except for O II) and it is spatially coincident with a gap in the molecular gas CO(1–0) (Gao et al. 1997). Interpretations for the origin of this radio emission comprise emission from supernova remnant (SNR) in molecular gas clouds with low density (e.g. Gao et al. 1997), radio emission from star formation triggered by the temporary enhanced density in the impact locus (e.g. Lamb et al. 1998), or emission from cosmic rays from star formation and supernovae explosions (e.g. Appleton et al. 2003).

This paper has been typeset from a TEX/LATEX file prepared by the author.